A hydrodynamic mechanism for cytoplasmic transfer between mammalian cells: Cell-projection pumping

Hans Zoellner[1,2*], Navid Paknejad[3], James Cornwell[1], Belal Chami[1], Yevgeniy Romin[3], Vitaly Boyko[3], Sho Fujisawa[3], Elizabeth Kelly[1], Garry W. Lynch[4], Glynn Rogers[1], Katia Manova[3], and Malcolm A.S. Moore[2]

[1] The Cellular and Molecular Pathology Research Unit, Oral Pathology and Oral Medicine, School of Dentistry, Faculty of Medicine and Health, The University of Sydney, Westmead Hospital, Westmead, NSW 2145, Australia
[2] Cell Biology, The Memorial Sloan Kettering Cancer Center, 430 E 67th St, RRL 717, New York, NY
[3] Molecular Cytology, The Memorial Sloan Kettering Cancer Center, 415-417 E 68 Street, ZRC 1962, New York, NY
[4] Sydney Medical School, Faculty of Medicine and Health, and Sydney School of Veterinary Science, Faculty of Science, The University of Sydney, NSW, 2006, Australia

Correspondence: Hans Zoellner
The Cellular and Molecular Pathology Research Unit, Oral Pathology and Oral Medicine, School of Dentistry, Faculty of Medicine and Health, The University of Sydney, Westmead Hospital, Westmead, NSW 2145, Australia
hans.zoellner@sydney.edu.au

ABSTRACT We earlier reported cytoplasmic fluorescence exchange between cultured human fibroblasts (Fib) and malignant cells (MC). Others report similar transfer via either tunneling nanotubes (TNT) or shed membrane vesicles and this changes the phenotype of recipient cells. Our current time-lapse microscopy showed most exchange was from Fib into MC, with less in the reverse direction. Although TNT were seen, we were surprised transfer was not via TNT, but was instead via fine and often branching cell projections that defied direct visual resolution because of their size and rapid movement. Their structure was revealed nonetheless, by their organellar cargo and the grooves they formed indenting MC. Discrete, rapid and highly localized transfer events, evidenced against a role for shed vesicles. Transfer coincided with rapid retraction of the cell-projections, suggesting a hydrodynamic mechanism. Increased hydrodynamic pressure in retracting cell-projections normally returns cytoplasm to the cell body. We hypothesize 'cell-projection pumping' (CPP), where cytoplasm in retracting cell-projections partially equilibrates into adjacent recipient cells via micro-fusions that form temporary inter-cellular cytoplasmic continuities. We tested plausibility for CPP by combined mathematical modelling, comparison of predictions from the model with experimental results, and then computer simulations based on experimental data. The mathematical model predicted preferential CPP into cells with lower cell stiffness, expected from equilibration of pressure towards least resistance. Predictions from the model were satisfied when Fib were co-cultured with MC, and fluorescence exchange related with cell stiffness by atomic force microscopy. When transfer into 5000 simulated recipient MC or Fib was studied in computer simulations, inputting experimental cell stiffness and donor cell fluorescence values generated transfers to simulated recipient cells similar to those seen by experiment. We believe CPP is a novel mechanism in mammalian inter-cellular cytoplasmic transfer and communication.

INTRODUCTION

We earlier described the exchange of membrane and cytoplasmic protein between cultured human fibroblasts (Fib) and malignant cells (MC) (1). Others have made similar observations, and describe this as via either tunneling nanotubes (TNT) or exosomes and other shed membrane vesicles, and this is often associated with changes in cell phenotype (2-17), while we have also seen phenotypic change (1, 18). Mitochondrial exchange has been considered particularly interesting (2, 4, 5, 19). TNT are long straight tube-like connections, typically suspended above the culture substrate, and establish cytoplasmic continuity between individual cells as a form of temporary partial fusion. They seem drawn out from pre-existing inter-cellular micro-fusions when touching cells migrate from one another, but may also form from fused adjacent filopodia (6-8, 12, 13, 20-22).

The current study was initially to examine the possibility that TNT accounted for our earlier observed inter-cellular transfer (1). Time-lapse confocal laser scanning microscopy (CLSM), however, revealed neither TNT or shed vesicles were involved, and led us to hypothesize what we believe to be a novel mechanism we term 'cell-projection pumping' (CPP) (Fig. 1). We now report these data, and describe and test our CPP hypothesis by a combination of: mathematical modelling; comparison of predictions from the model with experimental data; and comparison of computer simulation based on our mathematical model with experimental results.

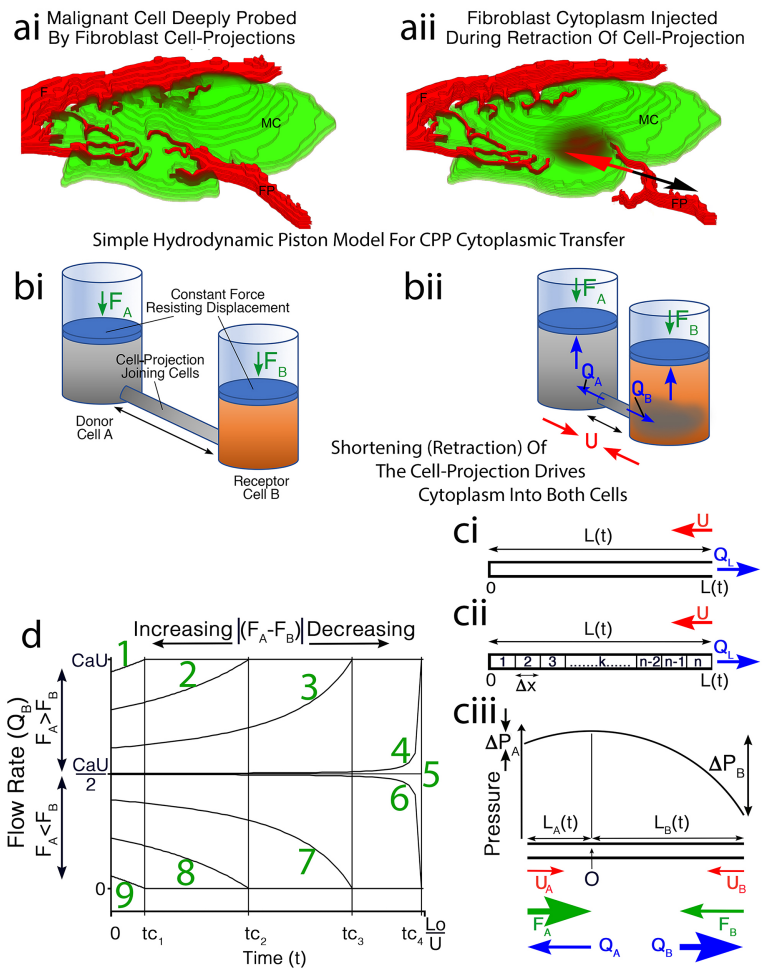

Fig. 1. *The CPP hypothesis.* ***(a)*** *Cartoon from a confocal image containing a MC deeply grooved by Fib (F) cell-projections (FP).* ***(aii)*** *If a micro-fusion establishes a transient inter-cellular cytoplasmic continuity, retraction of the cell-projection (black arrow) drives Fib cytoplasm into the MC (red arrow).* ***(bi)*** *This is modelled by piston-cylinders connected by a cylindrical tube (black arrow) containing fluid from the 'Donor Cell'.* ***(bii)*** *Shortening of the tube at constant rate U (red arrows) mimics cell-projection retraction, driving contents into both 'Donor' and 'Receptor Cells' at flow rates Q_A and Q_B respectively (blue arrows), against constant reactive resistance forces proportionate to cell stiffness (F_A, F_B, green arrows).* ***(ci)*** *A close-ended tube with length L(t) contracts at constant rate U (red arrow), generating flow of fluid within the tube of Q_L (blue arrow).* ***(cii)*** *Dividing into n cylinders of Δx length, with Δx approaching zero, relates L(t) to pressure and Q_L.* ***(ciii)*** *Two such tubes of lengths $L_A(t)$ and $L_B(t)$ are opened and joined at their origins (O), contracting at U_A and U_B ($U_A+U_B=U$) (red arrows), with flow (Q_A and Q_B, blue arrows) against constant forces (F_A and F_B, green arrows). Pressure is maximal at O, and equals F_A and F_B at the open ends, establishing ΔP_A and ΔP_B. Where $F_A>F_B$, $L_A(t)<L_B(t)$ and $Q_A<Q_B$; this reverses when $F_A<F_B$; while when $F_A=F_B$, $Q_A=Q_B$.* ***(d)*** *Q_B is plotted over time for retraction to extinction of a cell-projection in 9 separate circumstances where all variables are identical except for F_A and F_B, to generate 9 separate 'curves' as labelled. Notably, when $F_A>F_B$, there is a time (tc) when $L_A=0$, $Q_A=0$, and remaining flow is $Q_B=CaU$, where Ca= tube cross-sectional area. When $F_A<F_B$, $L_B=0$ at tc, so that $Q_B=0$, and remaining flow is Q_A. Decreasing F_A-F_B increases tc.*

With regard to CLSM results, it is important to appreciate necessity to use permanent labels, such as the fluorescent lipophilic markers 1,1'-dioctadecyl-3,3,3',3'-tetramethylindodicarbocyanine perchlorate (DiD) and 3,3'-dioctadecyloxacarbocyanine perchlorate (DiO), to demonstrate total

cytoplasmic transfer over time, because such labels accumulate and persist long after degradation of the originally labelled structures. By contrast, cell and organellar turn-over renders highly specific organellar or protein labels unreliable for detecting cumulative cytoplasmic transfer between cells (1). Also important, is that Fib have appreciably greater cell surface stiffness compared with MC (23). Further, punctate organellar labelling aids recognition of transfer events in time-lapse microscopy.

MATERIALS AND METHODS

Materials

All culture media including M199, DMEM-α Trypsin (0.25%)-EDTA (0.02%) and phosphate buffered saline (PBS), as well as Penicillin (10,000 U/ml)-Streptomycin (10,000 μg/ml) concentrate solution were prepared and supplied by the Memorial Sloan-Kettering Cancer Centre Culture Media Core Facility (New York, NY). Amphoteracin B was purchased from Life Technologies (Grand Island, NY). Gelatin was from TJ Baker Inc (Philipsburgh, NJ). Bovine serum albumin was from Gemini Bioproducts (West Sacramento, CA). Falcon tissue culture flasks, Atomic Force Microscopy (AFM) dishes and centrifuge tubes were purchased from BDBiosciences (Two Oak Park, Bedford, MA). Culture well coverslips were from Lab-Tek (Rochester, NY). Human dermal fibroblasts were from The Coriell Institute (Camden, NJ). SAOS-2 osteosarcoma cells were from the American Type Culture Collection (VA, USA). MM200-B12 melanoma cells from The Millennium Institute (Westmead, NSW, Australia). The fluorescent labels 1,1'-dioctadecyl-3,3,3',3'-tetramethylindodicarbocyanine perchlorate (DiD), 3,3'-dioctadecyloxacarbocyanine perchlorate (DiO), and Bacmam 2.0 Cell lights Nuclear-GFP baculovirus, were purchased from Molecular Probes by Life Technologies (Grand Island, NY) in the form of DiD and DiO Vybrant cell labelling solutions, and BacMam Cell Light transfection reagent. Paraformaldehyde (PFA) solution (32%) was purchased from Electron Microscopy Supplies (Hatfield, PA). A 6.1 μm spherical polystyrene AFM probe was purchased from NanoAndMore (Lady's Island, SC). The anti-fade reagent used was supplied by the Molecular Cytology core facility at Memorial Sloan Kettering Cancer Center.

Cell culture and fluorescent labelling

Cell culture was as earlier described (1, 18, 23, 24). Human dermal fibroblasts were cultured on gelatin coated surfaces (0.1% in PBS) in DMEM-α (15% FCS). Malignant cell (MC) lines were: melanoma MM200-B12 cultured in DMEM-α (10% FCS); and osteosarcoma cells SAOS-2 in M199 (10% FCS).

Labelling solutions of DiD for fibroblasts (1mM) and DiO for MC (2mM) were applied to cells for 30 min in the case of DiD, and 1h for DiO. Monolayers were washed prior to overnight culture and further washing before co-culture. In some experiments, MM200-B12 were transfected with green fluorescent protein (GFP) expressing baculovirus.

Co-culture conditions

Co-cultures were on gelatin (0.1% in PBS) coated surfaces with Fibroblasts seeded from 1 to 2 x 10^4 cells per cm^2 into either $25cm^2$ AFM culture plates (23), or culture well coverslips, and allowed to adhere overnight before labelling. MC were seeded at near confluence in either 25 cm^2 flasks or 6 well culture plates prior to labeling. MC were then harvested with trypsin-EDTA and seeded over fibroblasts in DMEM-α with BSA (4%) at 4 x 10^4 cells per cm^2 for up to 24 h co-culture.

Time-lapse CLSM

Eight separate visual fields of fibroblasts co-cultured with GFP labelled MM200-B12 were recorded for 25 h at 3 min intervals, representing 1.13 mm^2 culture surface area. Nine further separate visual fields of DiO pre-labelled MM200-B12 were recorded for 8 h 15 min at 5 min intervals and at slightly higher magnification, representing 0.76 mm^2 culture surface area. Monolayers were fixed with paraformaldehyde after co-culture. CLSM was by a Zeiss LSM 5Live line-scanning confocal microscope.

Combined atomic force and fluorescence microscopy

Paraformaldehyde fixed monolayers were stored in PBS at 4° C for combined fluorescence-AFM recordings of randomly selected cells (23). An Asylum Research MFP-3D-BIO atomic force microscope coupled with a Zeis Axio Observer A1 fluorescence microscope was used. Bright field and fluorescence images for both DiO and DiD channels were recorded prior to AFM scanning. A 1 μm AFM spherical polystyrene probe was used to record 16 x 16 points of force curves over 50 μm x 50 μm areas. Asylum Research, Software Version IX Young's modulus for each point by the Hertz model (23, 25). Height maps, bright field and fluorescence images were compared to localize discrete AFM measurement points to individual cells, and stiffness fingerprints were prepared (23).

Morphometric analysis and cell stiffness analysis

ImageJ open source software (http://imagej.net/Contributors) was used to segment and analyze fluorescence images of individual SAOS-2 and fibroblasts. Cell surface profile area was determined, while both Red and green fluorescence was summated for each cell. Fluorescence intensity in both fluorescence channels was expressed in 'Fluorescence Units' (summated fluorescence / surface profile area). Both fibroblasts and SAOS-2 were designated as belonging to one of two groups, being 'high' or 'low' labelling from the opposing cell type. Median AFM stiffness was determined for individual cells, while stiffness fingerprints were also made of cells according to group to address sampling limitations as earlier described (23). Prism 6.0e software (GraphPad Software Inc, La Jolla, CA) was used for statistical analysis.

Computer simulation of cytoplasmic and fluorescence transfer between fibroblast and SAOS-2 populations by CPP

Estimated cumulative distribution functions (ECDF) were developed in MATLAB (MATLAB by MathWorks Inc) from experimental median cell stiffness and fluorescence data. All MATLAB scripts are provided separately in Supplemental Information. ECDFs were then used to generate simulated populations of cells with distributions for stiffness and fluorescence closely approximating those of experimental data. This method was used to generate 5100 donor fibroblasts, 5100 donor SAOS-2, 5000 recipient SAOS-2, and 5000 recipient fibroblasts (Fig. 2).

Co-culture simulations were in MATLAB of random interactions between simulated donor and receptor cells, making random selection of values from lists of variables used to calculate CPP. Values loaded into these lists had distributions bounded by target minimum and maximum values, while target minima and maxima were established at the start of each simulation. Variables modelled in this way were: the number of Donor Cells A each Receptor Cell B could interact with; the number of transfer events each Receptor Cell B could have with each Donor Cell A; the flow rate (U) for each transfer event; the length at time 0 (L_0) of each cell-projection; the radius (r) of each cell-projection; and the viscosity of cytoplasm (η). Values for these parameters, were inferred on basis of CLSM observations, with exception of viscosity, which was taken from the literature (26, 27). The only exception to this was for the time permitted for each transfer event, the maximum of which is defined by L_0/U, and random choice of time was made from a pre-determined proportionate range between 0 and L_0/U. MATLAB script for simulations is provided below.

Average SAOS-2 and fibroblast cell height was determined from AFM data (3.89×10^{-6}m and 2.36×10^{-6}m respectively), while average SAOS-2 and fibroblast cell surface area (1.53×10^{-9}m^2 and 5.34×10^{-9}m^2 respectively) was by image analysis from separate experiments, and these data were used to calculate fluorescence from volume transfers.

Volume and fluorescence transfers for each simulated cell pairing were determined, and summated simulation results compared with experimental results. Maximal pressure generated during individual simulated CPP events was also recorded. Distributions of input variables as well as simulation outcomes were plotted in histograms (Figs. 3, 4). Data were analyzed using PRISM 7 (GraphPad Software Inc), and Mann Whitney U Tests where appropriate.

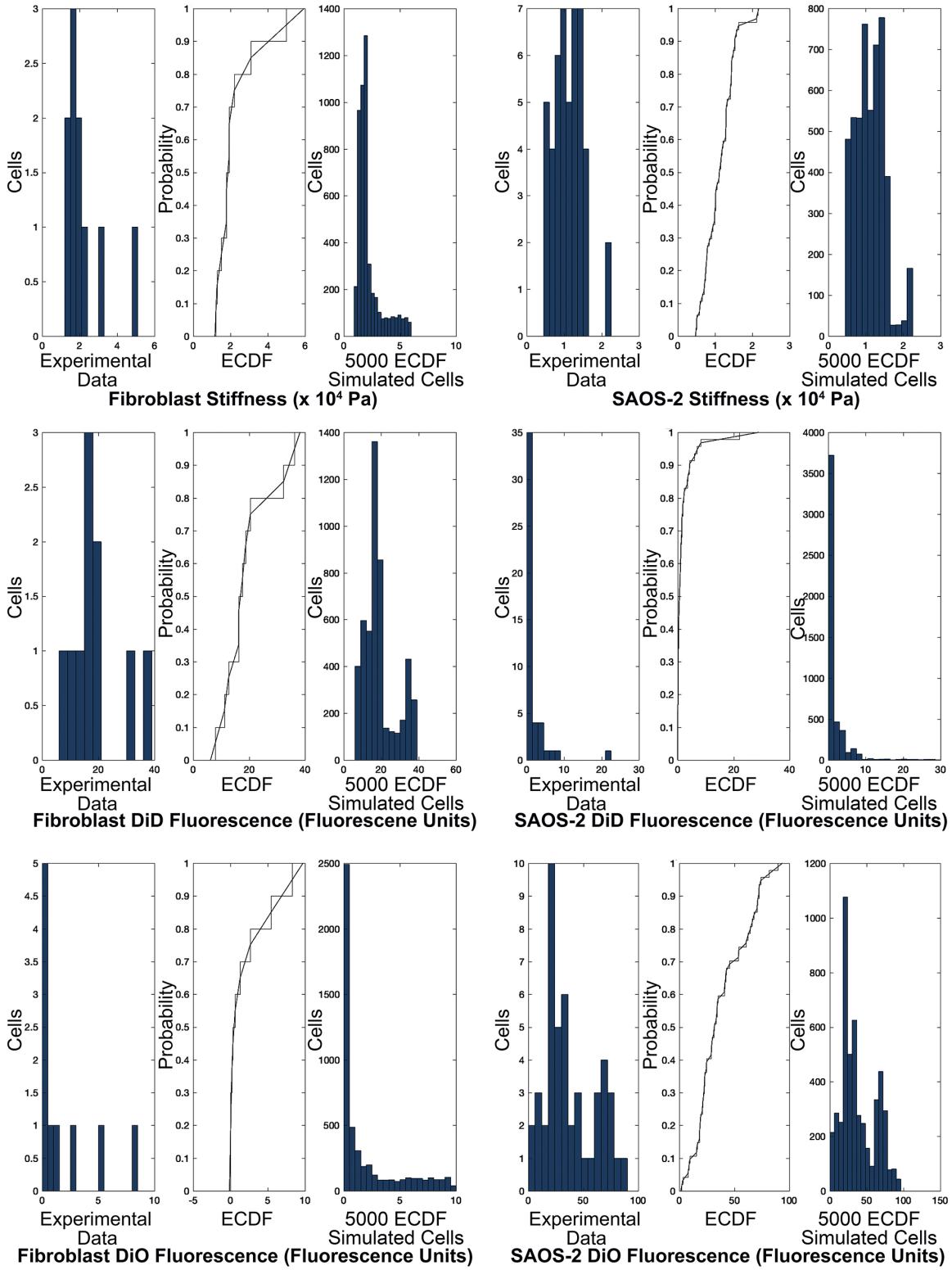

Fig. 2. *Histograms for experimental data for stiffness, DiD fluorescence and DiO fluorescence in co-cultured SAOS-2 and fibroblasts, as well as stair plots for the ECDF of these data with superimposed linear smoothing, and histograms for 5000 simulated cells generated by the ECDFs shown. Histograms of simulated cells had distribution profiles very similar to that of experimental data, despite the limited sampling available. Binning for histograms was: 3000 kPa for fibroblast stiffness; 1500 kPa for SAOS-2 stiffness; 3 DiD fluorescence units for fibroblast DiD; 1.5 DiD fluorescence units for SAOS-2 DiD; 0.5 DiO fluorescence units for fibroblast DiO; and 6 DiO fluorescence units for SAOS-2 DiO.*

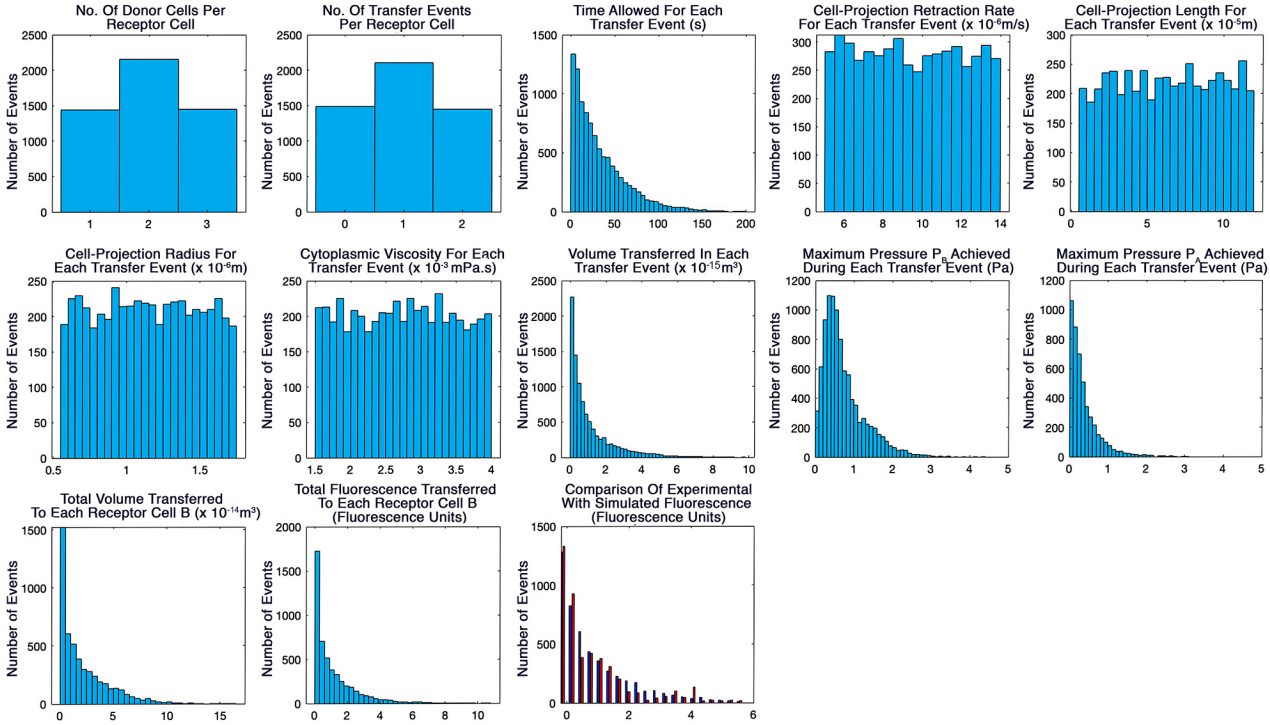

Fig. 3. *Histogram output of MATLAB script for simulation of CPP transfer from fibroblasts to SAOS-2 comparable to that seen by experiment (Fig. 13, Tables 1 and 2). Modest central tendency was seen for the number of donor cells receptor cells interacted with, as well as for the number of transfer events per receptor cell. Input variables for cell-projection retraction rate, length, radius and viscosity had essentially uniform distributions, while time permitted for transfer events was within range of time-lapse observations. Pressures generated during transfer were modest, while volume and fluorescence transfer was appreciable, closely approximating experimental fluorescence data.*

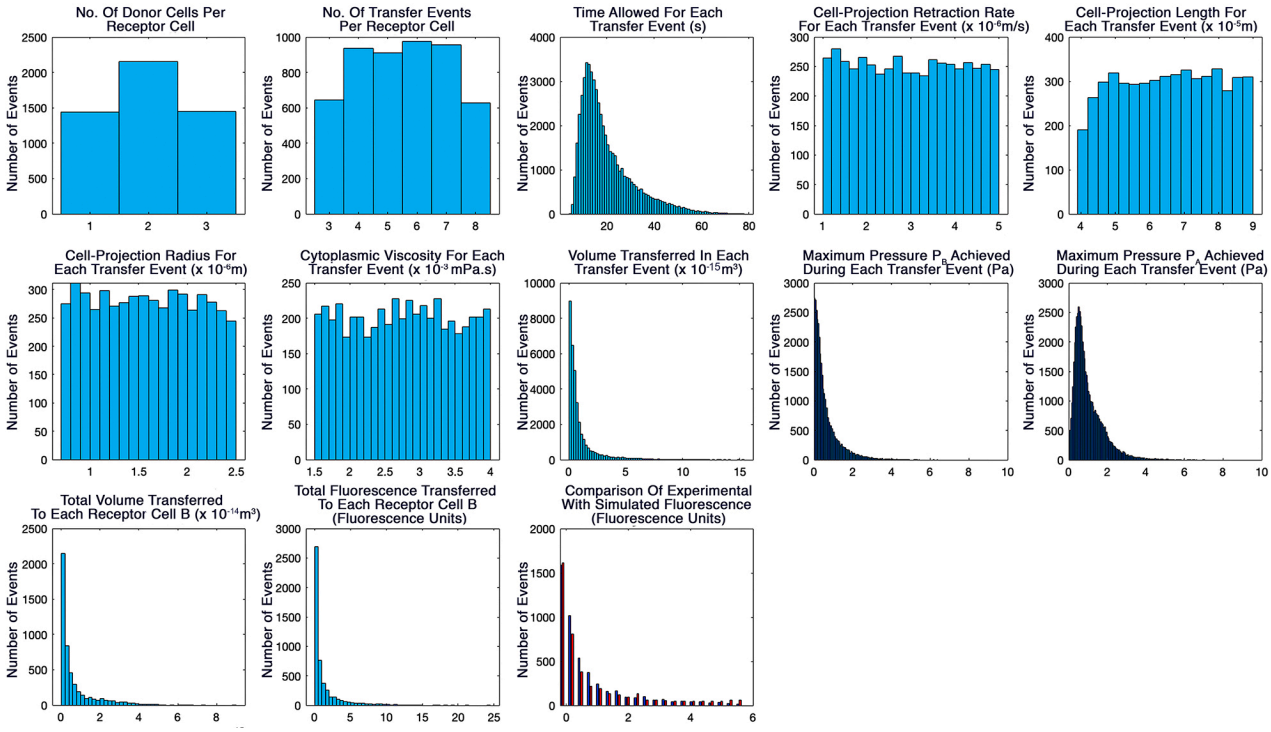

Fig. 4. *Histogram output of MATLAB script for simulation of CPP transfer from SAOS-2 to fibroblasts comparable to that seen by experiment (Fig. 13, Tables 1 and 2). Modest central tendency was seen for the number of donor cells receptor cells interacted with, as well as for the number of transfer events per receptor cell. Input variables for cell-projection retraction rate, length, radius and viscosity had essentially uniform distributions, while time permitted for transfer events was within range of time-lapse observations. Pressures generated during transfer were modest while volume and fluorescence transfer was appreciable, closely approximating experimental fluorescence data.*

RESULTS AND DISCUSSION

Transfer of organelles between Fib and MC

Organelles were clearly marked by both DiD and DiO. Organellar fluorescence overwhelmed plasma membrane labelling, so that plasma membranes were poorly defined by these labels. Obvious uptake of DiD labelled Fib organelles was in 11 of 106 DiO pre-labelled MC over 8 h 15 min co-culture, and 7 out of 71 GFP pre-labelled MC over 25 h co-culture (Figs. 5a, 6a,b; Supplemental movies S1, S2). Only once were DiO labelled organelles seen transferred from an MC to a Fib via broad cell-projections appearing as lamellipodia (Supplemental movie S3). While occasional large prominent Fib organelles were accepted by MC (Fig. 5a; Supplemental movie S1), most exchange was of smaller organelles, most readily seen when MC were labeled with DiO (Fig. 6; Supplemental movie S2). The precise identity of organelles transferred could not be defined from the images collected. However, the size and shape of the large organelles transferred was most consistent with mitochondria, and we have since verified that mitochondria can be exchanged by CPP in separate preliminary studies. We have no data on the specific identity of the smaller organelles below the size of mitochondria, and this awaits further study.

Fine Fib cell-projections distinct from TNT transferred Fib organelles to MC

Fib cell-projections transferring organelles to MC could not be precisely resolved because they moved between time-lapse frames and were mostly transparent by CLSM, but general form was nonetheless inferred from CLSM z-stack images. Fib cell-projections were clearly more stiff than MC, and formed deep grooves indenting MC surfaces. These often contained DiD labelled cargo (Figs. 5b,c; 6c,d, Supplemental movies S2 and S4). These fine Fib cell-projections appeared as tree-like branching networks terminating in filopodia-like extensions (Figs. 5b,c, 6c,d; Supplemental movies S2 and S4). Organellar transfer coincided with retraction events (Supplemental movies S1 to S3).

TNT differ markedly from the transferring cell-projections in the current study. Unlike the transient, fast-moving, short, and branching structures here seen to be mechanically supported by the culture surface or cells; TNT often persist hours, extend long distances, are non-branching, and are suspended free above the culture surface (6, 7, 12, 13, 20-22). Cytoplasmic transfer via cell-projections in the size range of filopodia seems a novel function. Some precedent is, however, established by filopodial transfer of melanosomes, but precise details of melanosome transfer remain uncertain and may be by phagocytosis (28-30).

It was clear organellar transfers must have involved transient cytoplasmic micro-fusions between adjacent cells similar to those involved in TNT formation (6-8, 12, 13, 20-22), but in this instance occurring in cell-projections. The basis for this remains unknown.

TNT, exosomes, fragmenting budding and non-specific label transfer did not account for observations

Occasional TNT were seen, but contributed little to observed transfers (Fig. 7). If shed membrane vesicles had played a significant role, the 'snowing' of vesicles onto cells would have produced slow, diffuse and near uniform uptake of label, independent of cell-projection retraction. Instead, however, we saw: highly localized organellar transfer, with label uptake varying greatly between immediately adjacent cells; brief and rapid bursts of organellar transfer between individual time-lapse frames; and an association between retraction of cell-projections and transfer events. As such, images were inconsistent with either a role for shed membrane vesicles, or phagocytosis of occasional Fib fragments. Admixture of organelles with differing label within cells suggested multiple uptake events, while intimate physical contact between Fib and MC was insufficient for diffusion of DiD into MC (Figs. 8, 9). We considered if donor cell fragments were 'torn off' and phagocytosed during cell-projection retraction. However, neither the budding of cell-projections, or formation of receptor cell surface spikes expected from such a mechanism, were ever seen.

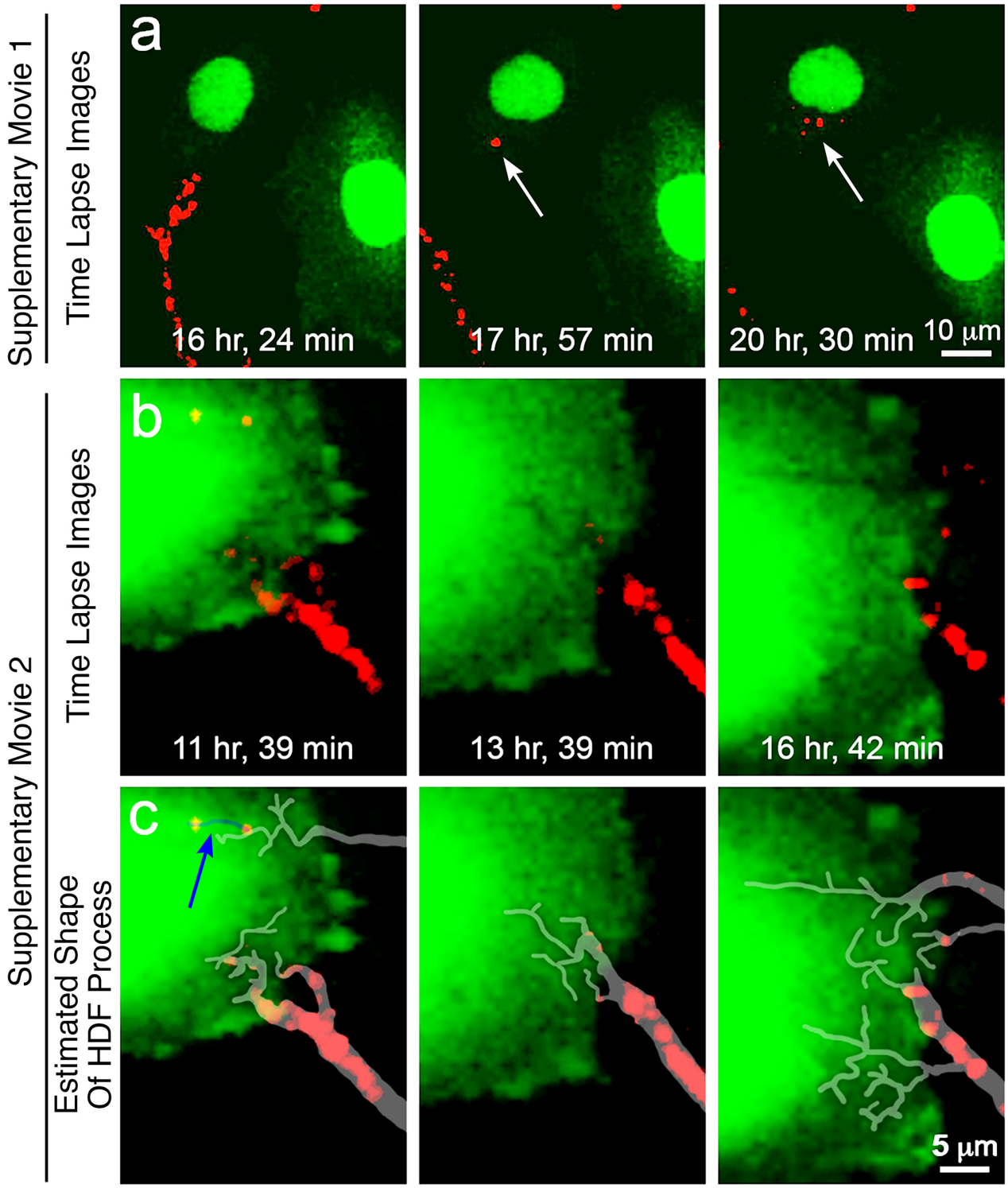

Fig. 5. *Frames from time-lapse CLSM recordings of Fib (pre-labelled DiD, red) co-cultured with MM200-B12 melanoma cells (GFP label); (Supplemental movies S1, S4)* ***(a)*** *A single large Fib organelle (red) was deposited into a green-labelled MM200-B12 cell (white arrow).* ***(b)*** *The location of Fib cell-projections was revealed by dark grooves made in the less stiff MM200-B12 cell, as well as by red-labelled organelles.* ***(c)*** *Inferred locations of cell-projections are marked with white transparency. One cell projection bearing red organelles speared into the MM200-B12 cell (blue transparency and arrow).*

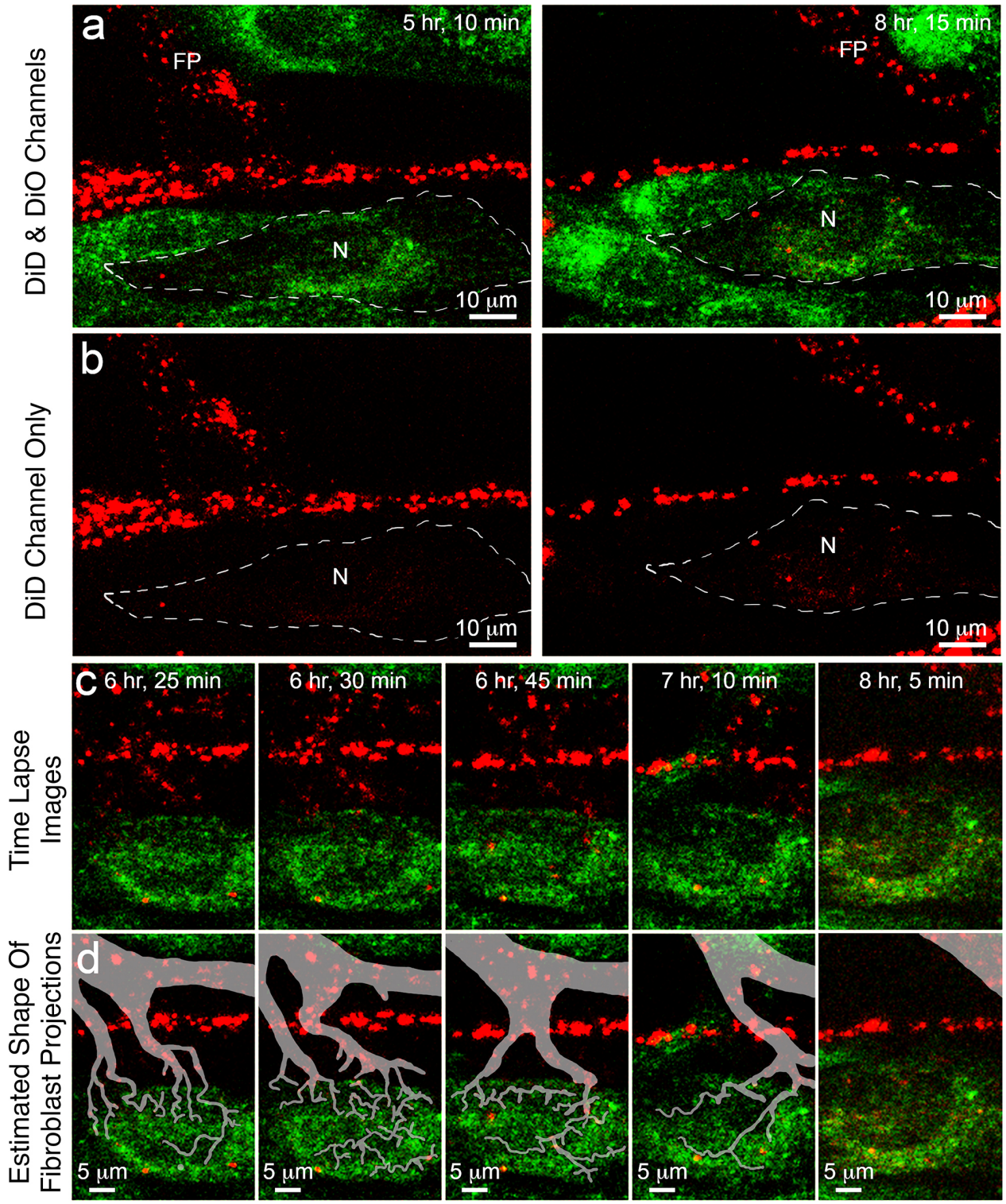

Fig. 6. *Frames from a time-lapse CLSM recording of Fib (pre-labelled DiD, red) co-cultured with MM200-B12 melanoma cells (pre-labelled DiO, green); (Supplemental movie S2).* ***(a, b)*** *A MC (white dashed outline) received red Fib organelles, readily seen when excluding the green channel (b).* ***(c)*** *This was from a broad Fib cell-projection (FP) that swept past the MC, indenting and grooving the recipient MC with numerous small branching cell-projections, all lost by 8 h 5min.* ***(d)*** *White transparency marks inferred locations of Fib cell-projections grooving the MC.*

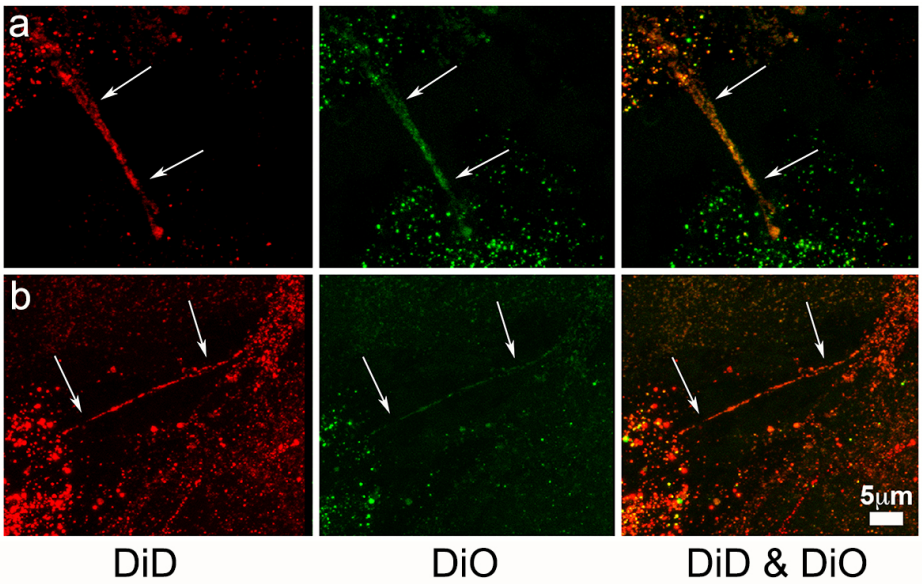

Fig. 7. *Flattened optical confocal microscopy projections of fibroblasts (pre-labelled with DiD-red) co-cultured for 24 Hr with MM200-B12 (pre-labelled with DiO-green), showing channels for DiD, DiO and both channels combined. TNT (white arrows) were occasionally seen, often connecting MC and bearing both DiD and DiO fluorescent markers. These did not, however, appear responsible for transfer of DiD labelled organelles from fibroblasts to MC. Similar to data shown above in Fig. 4, there was significant diversity in the extent of DiD labelling amongst organelles within individual cells, suggestive of frequent uptake of fibroblast DiD. Occasional DiO organelles with little or no DiD in MC otherwise heavily labelled with DiD, suggested recent uptake of DiO organelles from other MC, consistent with our earlier report (David et al, 2012, J Pathol 228:495-505).*

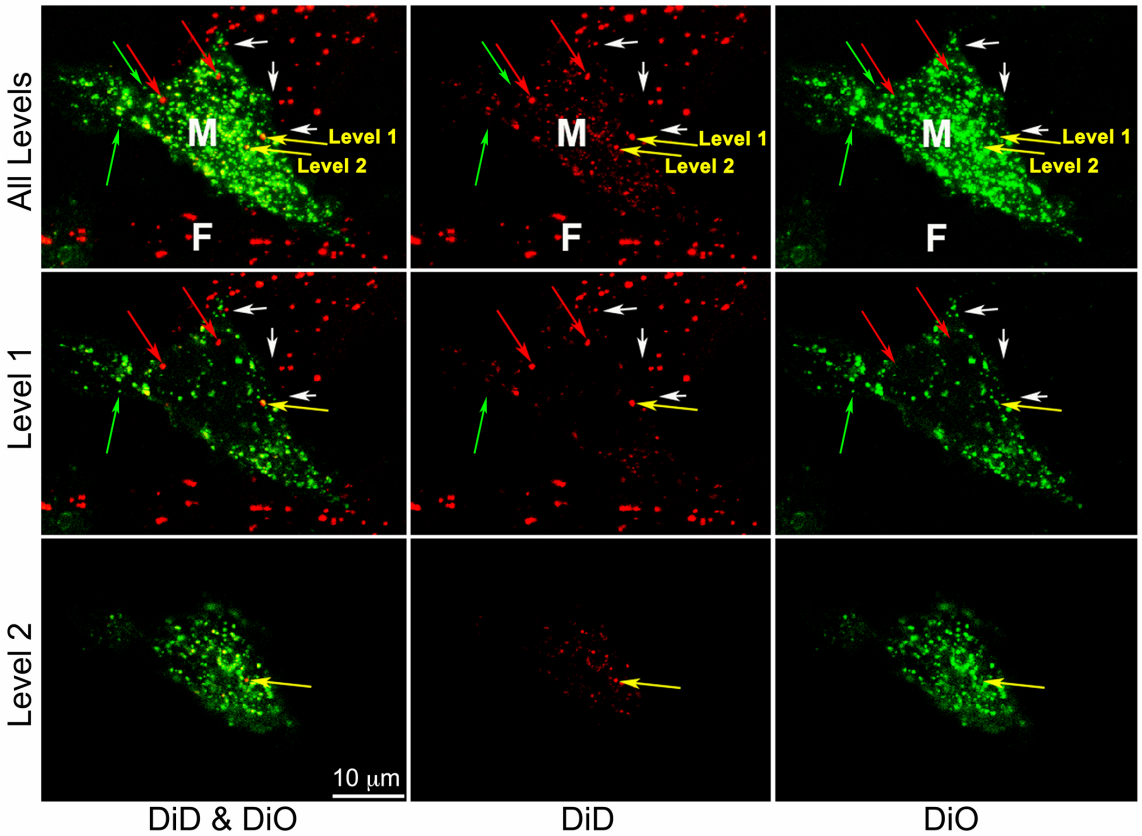

Fig. 8. *Flattened optical confocal microscopy projection and two optical levels of fibroblasts (pre-labelled with DiD-red) co-cultured for 24 Hrs with MM200-B12 (pre-labelled with DiO-green), showing channels for DiD and DiO alone or together. The MC shown (M) had many organelles bearing both DiO and DiD. Two fibroblasts (F) were in close association with this cell, and one of these had broad cell-projections approaching the MC (white arrows). Although many MC organelles had both DiO and DiD labelling, some organelles appeared to have only DiO (green arrow), and there were occasional organelles where only DiD labelling was seen (red arrows), both suggestive of recent acquisition of organelles from neighboring cells. In addition, organelles were noted that were primarily marked with DiD, but which also had some DiO marker (yellow arrows) indicative of label mixing following organellar membrane recycling. Examination of separate optical levels (Levels 1 and 2) confirmed that organelles with mixed DiD and DiO labelling marked with yellow arrows, had actual dual labelling and were not an artifact of two coincidentally overlapping and oppositely labelled organelles. Observations are consistent with frequent transfer of organelles from adjacent fibroblasts and MM200-B12.*

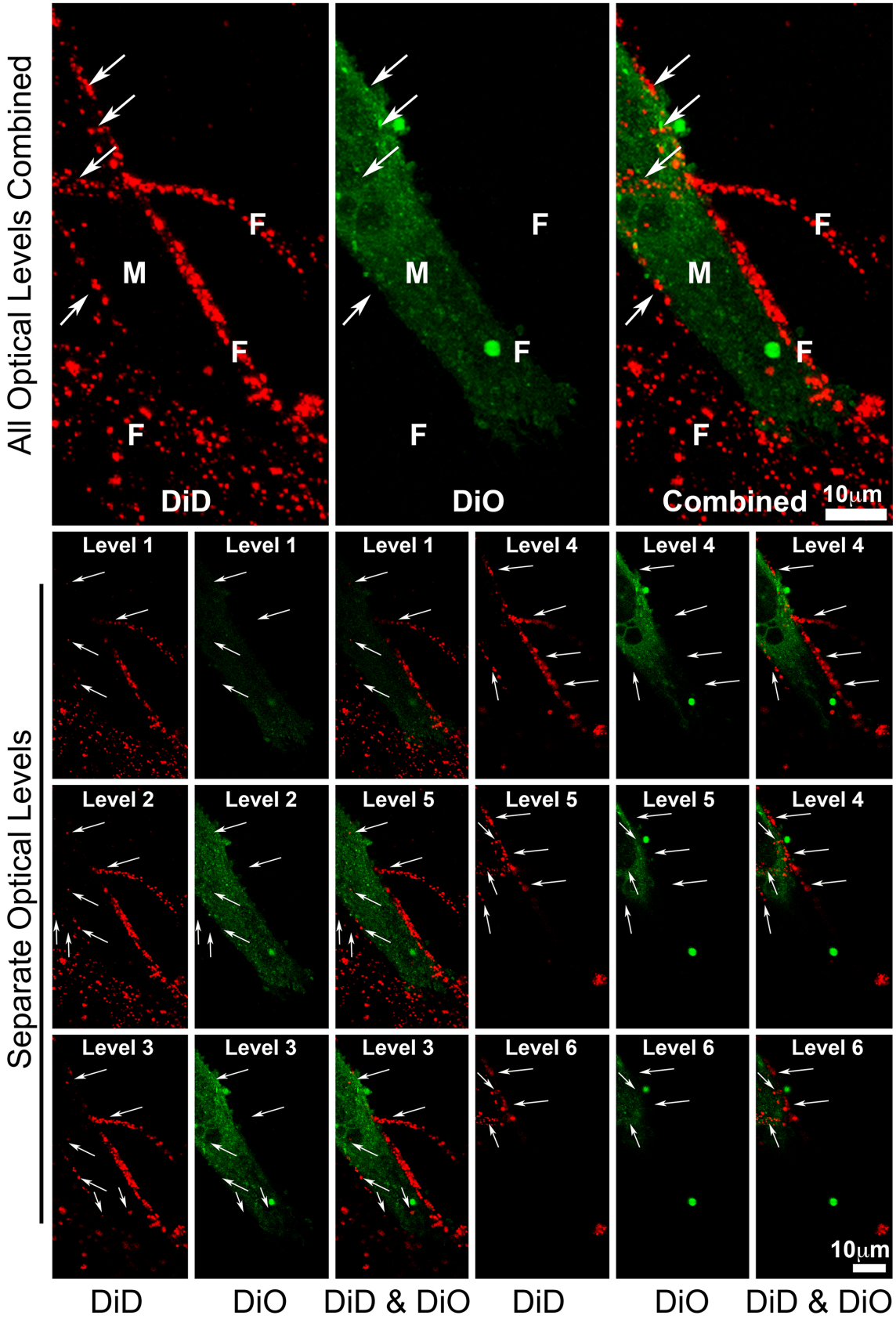

Fig. 9. *Flattened optical confocal microscopy projection and 6 optical levels of fibroblasts (pre-labelled with DiD-red) co-cultured with MM200-B12 (pre-labelled with DiO-green), showing channels for DiD and DiO alone and together. The MC (M) shown had no clear DiD (red) labelling, despite complex entwining of the cell by fibroblast (F) processes indenting and grooving the MC (white arrows), confirming that close physical association between MC and fibroblasts was insufficient for transfer of fibroblast DiD label into MC. This together with highly diverse fibroblast labelling of MC across co-cultures, was inconsistent with either non-specific label exchange or an appreciable role for exosomes or other shed membrane vesicles in the label transfer studied.*

The CPP hypothesis

Lacking clear resolution of the cell-projections responsible for transfer, we hypothesized CPP as a mechanism to account for our data. Transient increases in hydrodynamic pressure occur during retraction of cell-projections, thus returning cytoplasm to cell bodies. Micro-fusions that establish intercellular cytoplasmic continuities are known to occur early in TNT formation, and should such a micro-fusion exist between a cell-projection and neighboring cell during retraction, raised pressure within the cell-projection partially equilibrates by cytoplasmic flow into the neighbor. Because fluid flows towards least resistance, relative differences in cell stiffness affect the extent of transfer (Fig. 1a).

Assumptions and general approach to the mathematical model for CPP

CPP was described mathematically for a simple two chamber hydrodynamic system joined by a cylindrical connector, each chamber representing either Donor Cell A or Receptor Cell B, and the cylindrical connector representing a cell-projection from Cell A. We assume a constant rate of cell-projection retraction modelled by a constant rate of shortening for the cylindrical connector (U), that expels fluid into both Donor Cell A and Receptor Cell B at flow rates Q_A and Q_B respectively (Fig. 1b). Only Q_B was determined, since it is only Q_B which delivers cytoplasm to the opposing cell (Fig. 1b). Stiffness of donor Cell A and Receptor Cell B are considered proportionate to the reactive force of resistance to flow for Cells A and B respectively (F_A, F_B).

We applied the well described Hagen-Poiseuille relationships, where resistance to flow in a cylindrical tube (ρ) is given by Eq. 1, and the flow rate (Q) of a Newtonian fluid of viscosity (η) through a cylindrical tube of length (L) with radius (r), due to a pressure difference (ΔP) is as per Eq. 2 (31).

$$\rho = \frac{8\,\eta}{\pi \cdot r^{4}} \tag{1}$$

$$Q = \frac{\Delta P}{\rho \cdot L} = \frac{\Delta P \cdot \pi \cdot r^{4}}{8\,\eta \cdot L} \tag{2}$$

Bulk modulus was assumed to be negligible, as the fluid volumes exchanged are very small and cytoplasm was assumed to behave as a Newtonian fluid. Uptake of cytoplasm by receptor cells via CPP was assumed to have negligible effect on receptor cell cytoplasmic viscosity and cell stiffness. In absence of highly detailed structural data on the cell-projections that mediate CPP, and for purposes of necessary simplification, we have modelled cell projections as simple contracting cylindrical tubes. The hydraulic system is not confined but consists instead of two 'open' halves, each of which operates against a separate constant reaction force term in the form of a reaction pressure, F (F_A and F_B for Donor and Receptor cells respectively) (Fig. 1). Hence each half has a separate ΔP as also demanded by Pascal's law (32).

A central component of the CPP mechanism is resistance to cytoplasmic flow into each of the cells. We first considered if cells offered Hookean spring-like resistance to flow, but initial investigation demonstrated that this could not explain the experimental data. Instead, we have considered that cytoplasmic resistance behaves similarly to a Bingham plastic, where viscous flow occurs only when external force exceeds a defined yield point. We have assumed that for each cell, this yield point is proportional to the median stiffness of the cell measured by AFM, and we suggest this reflects disruption of bonds between either or both cytosolic or cytoskeletal elements (33). This contrasts with the simple viscous flow we assume for contents of cell-projections, on basis of the greatly simplified internal structure of cell-projections compared with cell bodies.

Consequently the effect of each cell on the flow from the projection can be accounted for by a single force term equivalent to the yield point (P^Y), of the cell cytoplasm. These force terms are the reaction pressures F_A and F_B. The yield point occurs when the deformation of the material under stress reaches a critical level. Assuming that this critical deformation is approximately the same for both cells, the yield point can be assumed to be proportional to the stiffness of the cell (S), as measured by AFM. If Z is the constant of proportionality then $P_A^Y = ZS_A$, and $P_B^Y = ZS_B$.

It seems reasonable to assume only modest effect of the simplifying assumptions outlined above, in diverging calculated estimations made in the current study from events in-vivo.

The mathematical approach is summarized below. A cylindrical tube with cross sectional area *(Ca)* is closed at one end and contains a Newtonian fluid. It undergoes constant contraction at rate *(U)* and has length $L(t)$ at time *(t)* as measured from '0' at it's origin (Fig. 1cii). By dividing the cylinder into n segments of length (Δx), considering the contribution of each segment to the total flow expelled from the contracting tube, and letting Δx approach 0, an expression relating flow to the position *(x)* along the tube is derived. Eqs. 1 and 2 are used to develop an expression for pressure drop along the length of the tube as detailed below.

The above outlined system is replicated, and one of these elements is rotated so that the two tubes abut end to end, sharing the same origin. This now represents a cell-projection joining Donor Cell A 'at left', with Receptor Cell B 'at right'. The origin represents a point (Po) where during contraction of the cell-projection, there is maximum pressure (P_{max}) and no flow. The length of tube between the origin and Donor Cell A is L_A, and that to Receptor Cell B is L_B, with rates of contraction U_A and U_B respectively. The entire system has length $L(t)$ and rate of retraction $U = U_A + U_B$ (Fig. 1ciii). The tube is open to Cells A and B, and flow in both directions is resisted by constant reaction pressures F_A and F_B (Fig. 1ciii). These reaction pressures are equal to the yield points P_A^Y and P_B^Y. Where $F_A=F_B$, then $L_A(t) = L_B(t) = L(t)/2$, and both cells receive equal flow at CaU/2. Where $F_A \neq F_B$ total flow into Receptor Cell B (Q_B) is given up to time *tc*.

The detailed basis for the impact of differences between F_A and F_B on determining both *tc* and Q_B are provided below. Note that $P_{max}(t)$ decreases with time (Fig. 1ciii), so where $F_A>F_B$, at time *tc*: $L_A(t)$ reaches 0; $P_{max}(t)$ reaches the yield point of cell A (P_A^Y) so that no further flow into Cell A is possible; and all remaining flow is to the right at Q_B = CaU, with the effect that Receptor Cell B receives more flow than Donor Cell A (Fig. 1ciii). The reverse applies when $F_A<F_B$, in that $P_{max}(t)$ reaches the yield point of Cell B at time *tc*, when L_B is extinguished, and all remaining flow is to Cell A at Q_A = CaU.

The behavior of the system is apparent from Fig. 1d, which shows Q_B as a family of 'curves' numbered 1 to 9 for varying values of F_A and F_B from $t = 0$ to $t = L_0/U$. Note that L_0/U defines the maximum time during which flow Q_B is possible, because the cell-projection is extinguished at that time. Similarly, Q_B cannot exceed CaU. For all values of F_A and F_B, total summated flow into both Cells A and B (Q_T) at any time *(t)* equates to CaU, such that $Q_T = Q_A + Q_B$ = CaU. Where $F_A = F_B$, $Q_A = Q_B$ = CaU/2 at all time points, to give a horizontal line crossing Fig. 1d (line drawn as 'curve' 5). 'Curves' 1 to 4 drawn above 'curve' 5 at CaU/2, show Q_B where $F_A > F_B$, while 'curves' 6 to 9 drawn below the horizontal at CaU/2 (5) show Q_B where $F_A < F_B$.

Considering Fig. 1ciii illustrating ΔP along the length of a cell-projection where $F_A > F_B$, both ΔP_A and ΔP_B reduce at the same rate while the cylinder shortens, but because $F_A > F_B$, ΔP_A is extinguished before ΔP_B, and this is at time tc when: F_A = maximum pressure at 'point 0' $L_A = 0$; flow into Cell A ceases; and all remaining flow is into Cell B at Q_B = CaU. In effect, 'point O' shifts to the left during contraction of the cell-projection, and time *tc* is the moment when 'point O' meets the opening of the cell-projection into Cell A. Please note that Fig. 1ciii illustrates circumstances when $F_A > F_B$, and relates to 'curves' above CaU/2 in Fig. 1d ('curves' 1 to 4). Where $F_A < F_B$, L_A is larger than L_B, and L_B extinguishes before L_A, to give 'curves' such as those illustrated in Fig. 1d below Q_B = CaU/2 ('curves' 6 to 9).

Although Fig. 1d shows 'curves' for Q_B with differing F_A and F_B, because $Q_A + Q_B$ = CaU, the curve for Q_A of the system is always given by symmetrical reflection of the 'curve' for Q_B about the horizontal at CaU/2. From this, if conditions are such that 'curves' 1, 2, 3 and 4 are for either Q_B or Q_A, then Q_A and Q_B are each respectively given by 'curves' 9, 8, 7 and 6. This is consistent with the paired symmetry of 'curves' 1, 2, 3 and 4 with respectively 9, 8, 7 and 6 expected for Q_B, where the absolute values for F_A-F_B are the same. Decreasing values for F_A-F_B drive the system towards perfect symmetry and constant Q_B at CaU/2. Increasing values for F_A-F_B drive the system towards the extremes for Q_B at either CaU or 0, dependent if F_A is larger or smaller than F_B respectively. These extreme values for Q_B are reached at time *tc*, which approaches 0 as F_A-F_B increases.

Integration of 'curves' for Q_B, gives total volumes transferred to Cell B throughout retraction of the cell-projection.

Details of modification of the Hagen-Poiseuille Equation accommodating differences in cell stiffness

Distribution of fluid during retraction of the cell-projection in Fig. 1a,b is influenced by the relationship between stiffness of Donor Cell A *(S_A)* and Receptor Cell B *(S_B)*, and this requires modification of the relationships described in Eqs. 1 and 2 for calculation of that portion of total flow distributed to Receptor Cell B *(Q_B)*.

Fig. 1ci shows a cylindrical tube of known length *L(t)* at time *(t)* as measured from '0' at it's origin which is closed and marked to the left, and in which there is contraction at a constant rate *(U),* as indicated in Eq. 3.

$$U = \frac{dL(t)}{dt} \tag{3}$$

The tube contains a Newtonian fluid, and is divided into n cylinders of equivalent length *(Δx)* as shown in Eq. 4, indexed from *n*=1 to n (Fig. 1cii).

$$\Delta x = \frac{L(t)}{n} \tag{4}$$

Because the tube undergoes a constant contraction, each cylinder also contracts by *UΔt/n* to displace a volume of fluid *(ΔV)* as in Eq. 5, where *Ca* is the cross-sectional area of the tube.

$$\Delta V = \frac{Ca \cdot U(\Delta t)}{n} \tag{5}$$

In this way, each cylinder donates an equivalent volume *(ΔV)* and flow rate increment *(Δq = ΔV/Δt),* to the total flow rate of the cylinder as in Eq. 6, substituting for *n* from Eq. 4.

$$\Delta q = \frac{Ca \cdot U}{n} = \frac{Ca \cdot U \cdot \Delta x}{L(t)} \tag{6}$$

Rearrangement of Eq. 6 gives Eq. 7.

$$\frac{\Delta q}{\Delta x} = \frac{Ca \cdot U}{L(t)} \tag{7}$$

As $n \to \infty$, $\Delta x \to 0$, so that the flow rate at *x*, *(Q(x)),* is given by Eq. 8.

$$Q(x) = \int_0^x \frac{Ca \cdot U}{L(t)} dx = \frac{Ca \cdot U \cdot x}{L(t)} \tag{8}$$

Note that the flow rate at the end of the tube where *x=L(t)* is *CaU* as expected (Fig. 1cii).

Let ρ be the resistance per unit length as given in Eq. 1, so that the resistance offered by any given small cylinder comprising the cell-projection *(ΔR)* is given by Eq. 9, and the pressure drop across the cylinder *($\Delta P_{\Delta X}$)* is given by Eq. 10 as per Eqs. 2 and 6; where rearrangement of Eq. 2 gives *ΔP = QρL and ρL equates to ΔR*, while *Δq* equates *Q* from Eq. 2 and is substituted with *CaU/n* from Eq. 6 .

$$\Delta R = \rho \cdot \Delta x \tag{9}$$

$$\Delta P_{\Delta X} = \Delta q \cdot \Delta R = \frac{Ca \cdot U}{n} \cdot \rho \cdot \Delta x \tag{10}$$

The pressure drop at any given cylinder *k* and *L=x* is given by Eq. 11, which can be rearranged to Eq. 12.

$$\Delta P_X = \frac{k \cdot Ca \cdot U}{n} \cdot \rho \cdot \Delta x \tag{11}$$

$$\frac{\Delta P_X}{\Delta x} = \frac{k \cdot Ca \cdot U \cdot \rho}{n} \tag{12}$$

Substituting for *1/n* from Eq. 4, and recognizing that $x = k\Delta x$ gives Eq. 13.

$$\frac{\Delta P}{\Delta x} = \frac{Ca \cdot U \cdot \rho \cdot k \cdot \Delta x}{L(t)} = \frac{Ca \cdot U \cdot \rho \cdot x}{L(t)} \tag{13}$$

Allowing $\Delta x \rightarrow 0$, gives the expressions in Eq. 14.

$$\frac{\Delta P}{\Delta x} \rightarrow \frac{dP}{d(x)} = \frac{Ca \cdot U \cdot \rho \cdot x}{L(t)} \tag{14}$$

From this, the pressure drop $P(x)$ at x, is given as expressions in Eq. 15.

$$P(x) = \int_0^x \frac{Ca \cdot U \cdot \rho \cdot x}{L(t)} dx = \frac{Ca \cdot U \cdot \rho \cdot x^2}{2 \cdot L(t)} \tag{15}$$

Consider the above outlined system now replicated, and one of these elements to be rotated so that the two tubes now abut end to end, with the origin x=0 being identical for both. This now represents a cell-projection joining Donor Cell A 'to the left', with Receptor Cell B positioned 'to the right'. The origin represents a point in the cell-projection (O) where during contraction of the cell-projection, there is maximum pressure and no flow, the origin functioning as an effective 'syringe stop' for flow in both directions. The length of tube between the origin and Donor Cell A is L_A, and that to Receptor Cell B is L_B (Fig. 1ciii), giving Eq. 16 for length at time t.

$$L(t) = L_A(t) + L_B(t) \tag{16}$$

The tube is open to Cells A and B, and flow out of the tube in both directions is resisted by constant reaction pressures F_A and F_B in Cells A and B respectively (Fig. 1ciii). These reaction pressures are equal to the yield points P_A^Y and P_B^Y which are proportional but not identical to the measured median cell stiffness of the Donor and Receptor cells (S_A and S_B), so that it may be helpful to read '*S*' for '*F*' when making reference to Fig. 1b,c.

Noting that U is constant, Eq. 16 gives Eq. 17 following simplification, where: $U = L/t$, $U_A = L_A/t$, and $U_B = L_B/t$.

$$U = U_A + U_B \tag{17}$$

The relationships in Eq. 18 follow from the above.

$$\frac{U_A}{U} = \frac{L_A(t)}{L(t)} \qquad \frac{U_B}{U} = \frac{L_B(t)}{L(t)} \tag{18}$$

If $P_{max}(t)$ is the pressure at the origin (O), then from Eq. 15, the pressure at x_B going to the right (P_R) is given by Eq. 19, ultimately reaching and being balanced by the hydrodynamic force resisting flow by Cell B (F_B) to the right, with pressure at x_A going left (P_L) reaching the hydrodynamic force resisting flow by Cell A (F_A) to the left (Eq. 19), as illustrated in Fig. 1ciii.

$$P_R(x) = P_{max}(t) - \frac{Ca \cdot U_B \cdot \rho \cdot x_B^2}{2 \cdot L_B(t)} \qquad P_L(x) = P_{max}(t) - \frac{Ca \cdot U_A \cdot \rho \cdot x_A^2}{2 \cdot L_A(t)} \tag{19}$$

Since $L_A = x_A$, and $L_B = x_B$, Eq. 19 simplify to Eq. 20.

$$P_R(x) = P_{max}(t) - \frac{Ca \cdot U_B \cdot \rho \cdot L_B(t)}{2} = F_B \qquad P_L(x) = P_{max}(t) - \frac{Ca \cdot U_A \cdot \rho \cdot L_A(t)}{2} = F_A \tag{20}$$

Rearrangement of Eq. 20 gives Eq. 21.

$$F_A + \frac{Ca \cdot U_A \cdot \rho \cdot L_A(t)}{2} = F_B + \frac{Ca \cdot U_B \cdot \rho \cdot L_B(t)}{2} \tag{21}$$

Substituting for L_A from Eq. 16 gives Eq. 22.

$$F_A + \frac{Ca \cdot U_A \cdot \rho \cdot (L(t) - L_B(t))}{2} = F_B + \frac{Ca \cdot U_B \cdot \rho \cdot L_B(t)}{2} \tag{22}$$

Substitution for: U_B from Eq. 17; U_A/U from Eq. 18; and L_A from Eq. 16, gives Eq. 23 for L_B.

$$L_B(t) = \frac{F_A - F_B}{Ca \cdot U \cdot \rho} + \frac{L(t)}{2} \tag{23}$$

The algebraic relationships leading to Eq. 23 apply equally to generate Eq. 24.

$$L_A(t) = \frac{F_B - F_A}{Ca \cdot U \cdot \rho} + \frac{L(t)}{2} \tag{24}$$

From Eqs. 23 and 24, when $F_A = F_B$, then $L_A(t) = L_B(t) = L(t)/2$, and both cells receive equivalent flow as expected from symmetry of the system. When $F_A > F_B$, a time is reached when $L_A(t)$ reaches 0 and all remaining flow is to the right, and Receptor Cell B receives more flow than Cell Donor Cell A (Fig. 1ciii), while the reverse applies when $F_A < F_B$.

Note that in Eq. 20 $P_{max}(t)$ decreases with time so where $F_A > F_B$, $P_{max}(t)$ reaches the yield point of cell A (P_A^Y) when $L_A = 0$, and no further flow into Cell A occurs; while where $F_A < F_B$, $P_{max}(t)$ reaches the yield point of cell B (P_B^Y) when $L_B = 0$, and no further flow into Cell B occurs.

Equation 25 follows from Eq. 8.

$$Q_B = \frac{Ca \cdot U \cdot L_B(t)}{L(t)} \tag{25}$$

To establish the total flow transferred to Receptor Cell B ($Q_B(t)$), $L_B(t)$ from Eq. 23 is substituted into Eq. 25, which with simplification gives Eq. 26.

$$Q_B = \frac{F_A - F_B}{\rho \cdot L(t)} + \frac{Ca \cdot U}{2} \tag{26}$$

Because U is constant, $L(t)$ is given by Eq. 27, and substitution for $L(t)$ in Eq. 26 gives Eq. (28).

$$L(t) = L_0 - U \cdot t \tag{27}$$

$$Q_B = \frac{F_A - F_B}{\rho \cdot (L_0 - U \cdot t)} + \frac{Ca \cdot U}{2} \tag{28}$$

Note that Eq. 28 can only apply while $(F_A - F_B)/\rho(L_0 - Ut) \leq CaU/2$, because once $(F_A - F_B)/\rho(L_0 - Ut) = CaU/2$, $L_A = 0$ and $L_B = L$ where $S_A > S_B$, with all remaining flow being to the right into Receptor Cell B at a rate of $Q_B = CaU$. We define the time at which this occurs as time tc, which is given by Eq. 29. Please note that where $S_A < S_B$, $L_B = 0$ and $L_A = L$ and all remaining flow is to the left into Donor Cell A after time tc.

$$\frac{F_A - F_B}{\rho \cdot (L_0 - U \cdot tc)} = \frac{Ca \cdot U}{2} \tag{29}$$

Expansion, rearrangement and simplification of Eq. 29, gives Eq. 30 for *tc*, where the absolute value of second term on the right is required to accommodate occasions when $F_A < F_B$.

$$tc = \frac{L_0}{U} - \left| \frac{2(F_A - F_B)}{Ca.\rho \cdot U^2} \right| \tag{30}$$

Fig. 1d is a graphical representation of Q_B from $t = 0$ to $t = L_0/U$ at which time $L_B = 0$ and no further flow Q_B is possible. When $F_A > F_B$, Eq. 28 for Q_B applies for $t \leq tc$, and $Q_B = CaU$ for $tc < t < L_0/U$. Increasing values of $(F_A - F_B)$ reduce *tc,* while as $(F_A - F_B)$ approaches 0, *tc* approaches L_o/U and Q_B approximates $CaU/2$ from above for increasing time when $F_A > F_B$, and from below when $F_A < F_B$. Also, when $F_A < F_B$, Eq. 28 predicts that Q_B approaches 0 as *t* approaches *tc*, after which Q_B remains 0 due to exhaustion of L_B to 0 at *tc.*

Calculation of volumes transferred

Volumes transferred can be calculated by integration of curves for Q_B such as show in Fig. 1d. Let the total volume transferred to Receptor Cell B be V_B.

Where $F_A > F_B$, the relationships outlined above determine $V_B(t)$ as per Eq. 31, where the first term relates to those parts of the curves in Fig. 1d where Q_B is rising, and the second term relates to the following horizontal parts of curves once Q_B reaches CaU.

$$V_B(t) = \int_0^{tc} \left(\frac{Ca \cdot U}{2} + \frac{F_A - F_B}{\rho \cdot (L_0 - U \cdot t)}\right) dt + \int_{tc}^{L_0/U} (Ca \cdot U)\ dt \tag{31}$$

Similarly, where $F_A < F_B$, $V_B(t)$ is given by Eq. 32, where all curves illustrated in Fig. 1d reduce towards $Q_B = 0$, and only one term is required for integration.

$$V_B(t) = \int_0^{tc} \left(\frac{Ca \cdot U}{2} + \frac{F_A - F_B}{\rho \cdot (L_0 - U \cdot t)}\right) dt \tag{32}$$

Also, where $F_A = F_B$, $V_B(t)$ is given by Eq. 33.

$$V_B(t) = \int_0^{L_0/U} \left(\frac{Ca \cdot U}{2}\right) dt \tag{33}$$

To aid integration in Eqs. 31 and 32, define *w(t)* as in Eq. 34, such that when $t = 0$, $w = L_0$; and when $t = tc$, $w = L_0 - Utc$.

$$w(t) = L_0 - U \cdot t \tag{34}$$

Differentiating Eq. 34 gives Eq. 35.

$$dw = -U \cdot dt \tag{35}$$

From this, the second term in Eqs. 31 and 32 can be expressed and integrated with regard to w as in Eq. 36, where ln*(w)* is the natural logarithm of *w*. Substitution of Eq. 34 into Eq. 36 gives the expression in Eq. 37.

$$-\frac{1}{U} \int_{L_0}^{(L_0 - U \cdot tc)} \left(\frac{F_A - F_B}{\rho \cdot w}\right) dw = -\frac{F_A - F_B}{\rho \cdot U} \cdot \ln(w) \Big|_{L_0}^{L_0 - tc \cdot U} \tag{36}$$

$$= -\frac{F_A - F_B}{\rho \cdot U} \cdot \begin{cases} \ln(\frac{L_0 - U \cdot t}{L_0}), & if \;\; t \leq tc \\ \ln(\frac{L_0 - U \cdot tc}{L_0}), & if \;\; t > tc \end{cases} \tag{37}$$

From Eq. 37, the integral of $V_B(t)$ for $0 < t < tc$ in Eqs. 31 and 32 is as in Eq. 38.

$$\frac{Ca \cdot U \cdot t}{2} - \frac{F_A - F_B}{\rho \cdot U} \cdot \ln(\frac{L_0 - U \cdot t}{L_0}) \tag{38}$$

Combining the result of Eq. 38 with Eqs. 31, 32, and 33 provides Eqs. 39 to 42 used to determine V_B for all conditions tested in the current study, where: *tm* is the time at which any given contraction event ceases; and *Z* is a constant correcting for the assumed linear relationship between median cell stiffness and both F_A and F_B, such that $ZS_A=F_A$, and $ZS_B=F_B$.

Where $S_A>S_B$, and *tm* is $\leq tc$, V_B is calculated by Eq. 39.

$$V_B = \frac{Ca \cdot U \cdot tm}{2} - \frac{Z \cdot (S_A - S_B)}{\rho \cdot U} \cdot \ln(\frac{L_0 - U \cdot tm}{L_0}) \tag{39}$$

Where $S_A>S_B$, and *tm* is $> tc$, V_B is calculated by Eq. 40, noting that *tm* cannot exceed L_0/U.

$$V_B = \frac{Ca \cdot U \cdot tc}{2} - \frac{Z \cdot (S_A - S_B)}{\rho \cdot U} \cdot \ln(\frac{L_0 - U \cdot tc}{L_0}) + Ca \cdot U \cdot (tm - tc) \tag{40}$$

Where $S_A<S_B$, and *tm* is $\leq tc$, V_B is calculated by Eq. 39.
Where $S_A<S_B$, and *tm* is $> tc$, V_B is calculated by Eq. 41.

$$V_B = \frac{Ca \cdot U \cdot tc}{2} - \frac{Z \cdot (S_A - S_B)}{\rho \cdot U} \cdot \ln(\frac{L_0 - U \cdot tc}{L_0}) \tag{41}$$

Where $S_A=S_B$, V_B is calculated by Eq. 42.

$$V_B = \frac{Ca \cdot U \cdot tm}{2} \tag{42}$$

Calculation of pressures at time zero

Maximum pressure drop at time zero for Cell A and Cell B, was calculated from Eq. 15, substituting L_A and L_B for *L(t) and x,* to give ΔP_A and ΔP_B respectively.

Predictions from the mathematical model

Examination of Eqs. 2 and 28 identifies variables that when raised, predict increased Q_B (ΔP, F_A-F_B, Ca, U, r) and decreased Q_B (ρ, η, L_0). Of these, by far the most influential variable is *r*, reflecting the power function in Eq. 2.

Imagine two cell populations D and E, exchanging cytoplasm with each other via CPP. Variability in cell stiffness within each of the cell populations D and E is represented by a range of values for F_D and F_E respectively. Assume that there are an equal number of transfers from Cells D to E, as there are from E to D, and that all other variables for CPP in Eq. 28 are the same for all transfers from Cells D to E, as they are for transfers from Cells E to D.

Considering Fig. 1d, in the particular circumstance where the range and distribution of values for F_D and F_E are identical, if all other relevant variables are also identical, then transfers from Cells D to E are essentially mirrored by transfers from Cells E to D, and 'curves' for Q_B into both populations will be as often above the horizontal ('curves' 1, 2, 3 and 4) as below ('curves' 6, 7, 8 and 9). No preference in the distribution of volume transfers would be seen between the two cell populations.

On the other hand, if Cells D have a distribution of cell stiffness values such that F_D is often greater than F_E, then there will be skewing of the frequency with which different 'curves' for Q_B arise. For CPP transfers from Cells D to E, amongst the 'curves' 1 to 9 drawn in Fig. 1d, the frequency of their occurrence would reduce with increasing 'curve number'. This would contrast with CPP transfers from Cells E to D, where the frequency of occurrence of 'curves' drawn 1 to 9 in Fig. 1d would increase with increasing 'curve number'. Because volumes transferred reduce with increasing 'curve number' as drawn in Fig. 1d, and also because there is skewing of 'curve number' downwards for transfers from Cells D to E, as opposed to skewing of 'curve number' upwards for transfers from Cells E to D, the model predicts that there is preferential CPP transfer from populations of cells with high cell stiffness, to populations of cells with low cell stiffness.

A further prediction can also be made from Fig. 1d. Imagine two cells, A and B connected as in Fig. 1b, and experiencing CPP till extinction of the cell projection. In the first instance, let F_A be very much greater than F_B, so that the 'curve' drawn as '1' in Fig. 1d shows Q_B to be at the maximum of CaU for most of the time during which cell-projection retraction occurs. Let all conditions be the same, except that F_B is increased, initially modestly so that 'curve' 2 now shows Q_B, and then in separate cases where FB is further increased to generate 'curves' 3 and 4 for Q_B. Once F_B has risen to be equal to F_A, 'curve' 5 for Q_B appears as a horizontal at CaU/2. Allowing F_B to increase further, generates first 'curve' 6, and then 'curves' 7 to 9 as F_B rises further still. Integrating curves 1 to 9 shows that the total volume transferred by CPP reduces with increasing F_B. From this, an inverse relationship is predicted between the stiffness of individual cells within any given population of receptor cells, and the volume of cytoplasm acquired by CPP from the partner donor cell population. These predictions are illustrated in computer simulations shown in Fig. 10 showing how cell stiffness relates to volume and fluorescence transfer.

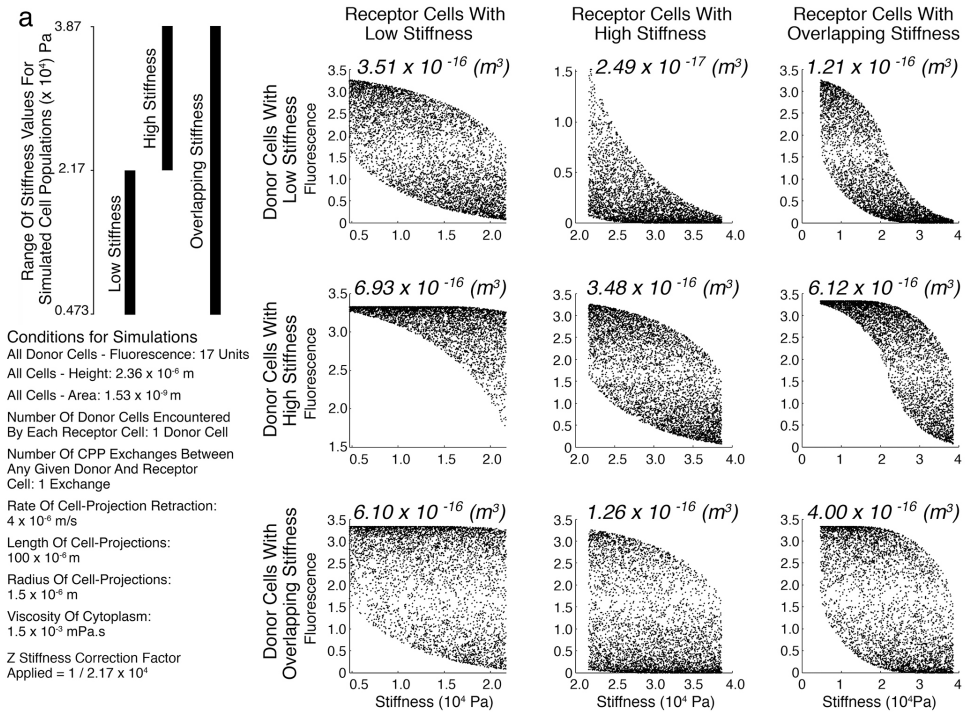

Fig. 10. *Scattergrams from computer simulations showing the relationship between stiffness of individual receptor cells and fluorescence acquired from donor cells, where stiffness of the two cell populations is varied, as well as the median CPP volume exchange for each simulation expressed in units of m³ a) Three cell populations were modelled: 'Low Stiffness' where stiffness had the same range as determined by experiment for SAOS-2; 'High Stiffness' with an equivalent range of stiffness, but where the lowest stiffness value was the same as the highest for the 'Low Stiffness' cell population; and 'Overlapping Stiffness' with stiffness covering the full range of both 'High' and 'Low' stiffness cell populations. 5100 donor and 5000 receptor cells were modelled in all simulations, with each cell assigned a unique stiffness value in equidistant steps from lowest to highest stiffness. The order of cells was randomized prior to simulations. For helpful simplicity, a single CPP event was modelled for each cell, and all variables were identical for all CPP exchanges as indicated. As predicted from the mathematical model, considering pairings between each of the three cell populations modelled, there was preferential CPP transfer from more to less stiff cell populations, as reflected by higher median CPP volume exchanges. Also, although the shape of data clouds varied between donor-receptor pairings and identity of receptor cells, negative correlation between receptor cell stiffness and CPP fluorescence uptake was a consistent feature, as expected from the mathematical model. While more complex distributions for input variables will generate more complex data clouds, these simulations support generality for these two principal predictions from the mathematical model.*

We earlier showed that Fib have higher but overlapping stiffness compared with SAOS-2 (23), so that based on the above, the mathematical model predicts: a) preferential CPP transfer of fluorescent label from Fib to SAOS, compared with transfer from SAOS-2 to Fib; b) an inverse correlation between SAOS-2 stiffness and CPP fluorescence uptake from co-cultured Fib; and c) an inverse correlation between Fib stiffness and CPP fluorescence uptake from co-cultured SAOS-2.

Experimental measurement of cell stiffness and fluorescence in co-cultured cells satisfied predictions of the mathematical model

We studied SAOS-2, because most of our earlier and subsequent work on phenotypic effects of transfer has been with this cell line (1, 18, 24, 34). Fluorescence microscopy of a co-culture of Fib with SAOS-2, revealed the most evident transfer of fluorescent label was from Fib to SAOS-2, with less obvious fluorescence transfer from SAOS-2 to Fib (Fig. 11a). Although stiffness varied greatly across surfaces of individual cells, stiffness fingerprints confirmed Fib were stiffer and had lower cell height compared with SAOS-2 (Mann Whitney U Test, $p < 0.0001$) (Fig. 11b,c,d). These data thus satisfied the prediction that there would be preferential CPP transfer of fluorescent label from Fib to SAOS, compared with transfer from SAOS-2 to Fib.

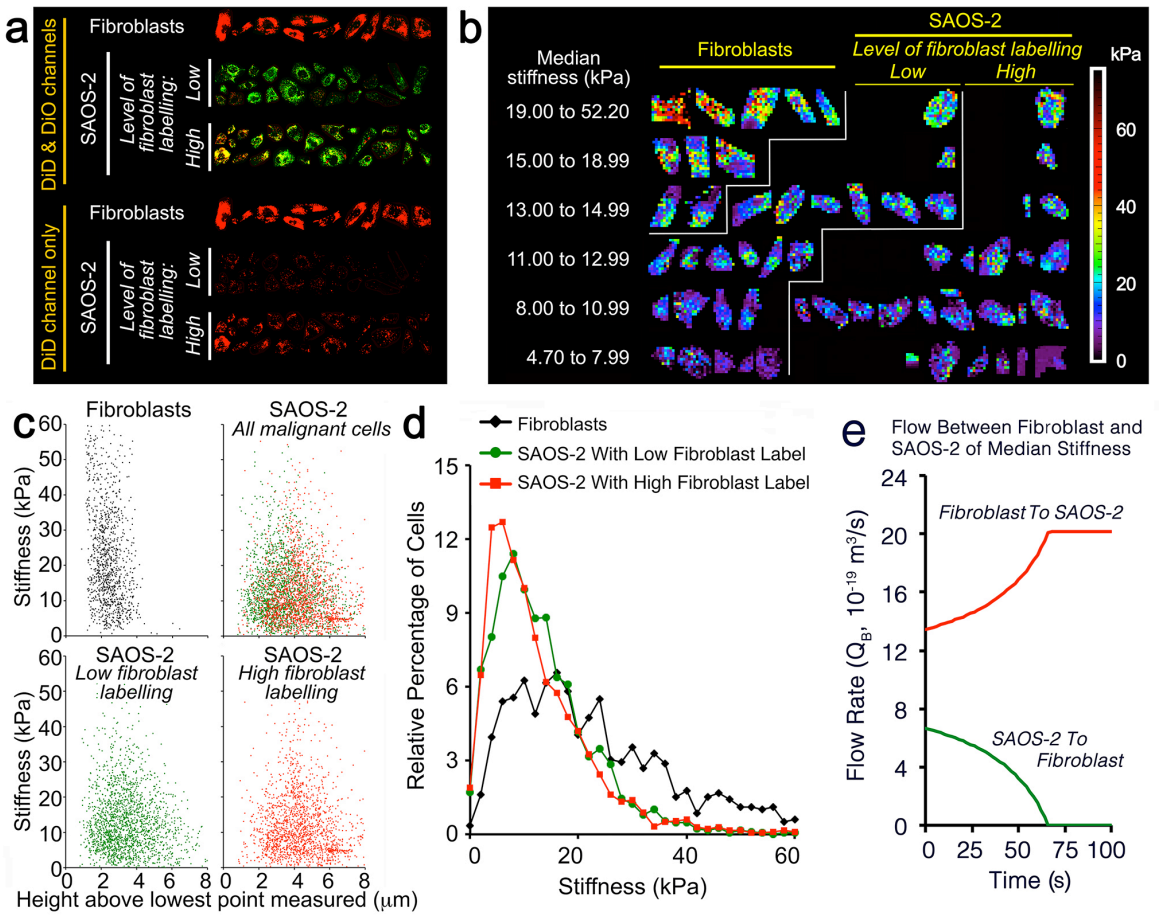

Fig. 11. *Relationship between cell stiffness and fluorescence in SAOS-2 (pre-labelled DiO, green) co-cultured for 24 h with Fib (pre-labelled DiD, red).* ***(a)*** *DiD levels were quantitated to identify Fib, SAOS-2 with high Fib label, and SAOS-2 with low Fib label.* ***(b)*** *Cells are grouped and separated by stair-lines according to identity as being either: Fib (top left group); SAOS-2 with low Fib labelling (middle group); or SAOS-2 with high Fib labelling (right hand group). Within each group, cells are arranged in tiers of increasing median AFM stiffness. Median AFM stiffness varied greatly within these groups, although Fib were generally stiffer than SAOS-2, while SAOS-2 with high Fib label were usually less stiff than SAOS-2 with low Fib label.* ***(c)*** *Stiffness fingerprints supported this, showing Fib (black dots) had greater stiffness and lower cell height than SAOS-2 (red and green dots) (Mann Whitney U Test, $p < 0.0001$). Further, stiffness of SAOS-2 with low Fib labeling (green dots) was higher than for SAOS-2 with high Fib labelling (red dots), and the reverse applied for height measures (Mann Whitney U Test, $p < 0.0004$).* ***(d)*** *Relative percentage distribution plots binned at 2 kPa for stiffness.* ***(e)*** *CPP was modelled between a Fib and SAOS-2, each of median cell stiffness, examining exchange from Fib to SAOS-2 (red), as well as from SAOS-2 to Fib (green). Results were consistent with the CPP hypothesis.*

Label transfer varied amongst SAOS-2, with some SAOS-2 having high and others negligible Fib labeling (Fig. 11a). SAOS-2 with high Fib labeling had lower stiffness compared with SAOS-2 with low Fib labeling (Mann Whitney U Test, $p < 0.0004$) (Fig. 11b,c,d). In addition, higher uptake of fluorescence correlated with greater cell height (Mann Whitney U Test, $p < 0.0004$). These data thus satisfied the further prediction of an inverse correlation between SAOS-2 stiffness and CPP fluorescence uptake from co-cultured Fib.

Fig. 11e shows CPP flow rates for transfer between a Fib and SAOS-2 cell, each with median stiffness (18,765 Pa 11,181 Pa respectively), considering each cell in turn as donor or receptor, and applying biologically reasonable assumptions for: cell-projection retraction rate (1×10^{-6}m/s), viscosity (2.5×10^{-3} Pa.s), length at time zero (100 μm), and radius (0.8 μm) of the cell-projection. Significant flow was calculated from the mathematical model, and transfer from the Fib exceeded that from the SAOS-2, consistent with predicted preferential CPP transfer from Fib to SAOS-2.

Similar to observations in SAOS-2 (Fig. 11), uptake of fluorescence from SAOS-2 by Fib was negatively correlated with Fib cell stiffness, and there was also a positive correlation with cell height (Mann Whitney U Test, $p < 0.0001$) (Fig. 12). This was consistent with the prediction of inverse correlation between Fib stiffness and CPP fluorescence uptake from co-cultured SAOS-2.

Experimental results thus satisfied all predictions from the mathematical model.

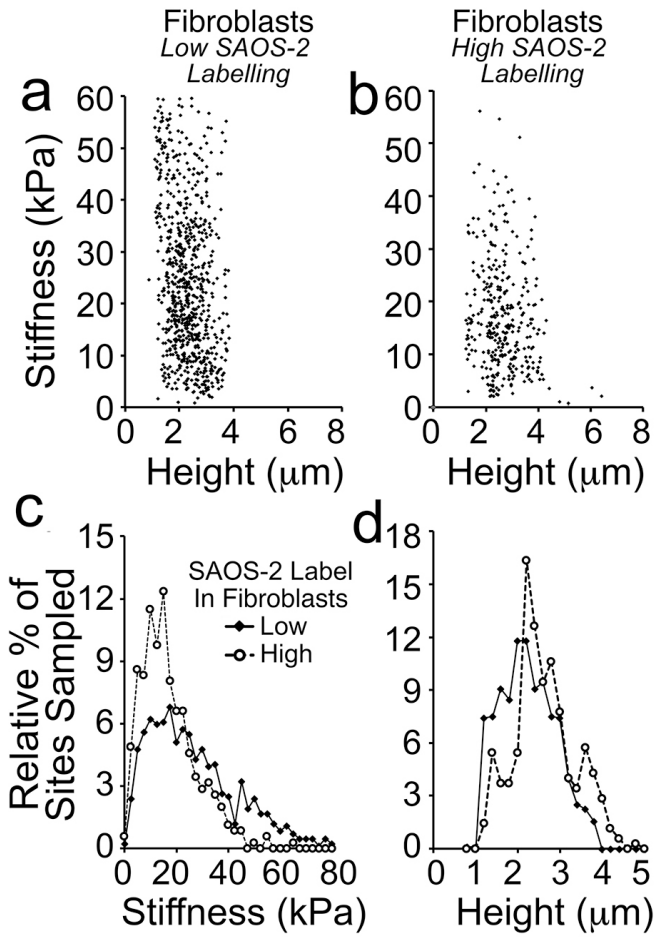

Fig 12. *Stiffness fingerprints and proportional distribution plots of AFM stiffness and height records for Fib in co-culture with DiO pre-labelled SAOS-2 according to level of SAOS-2 labelling* ***(a,b)*** *Fib with low SAOS-2 labelling had higher stiffness and lower cell height measurements (a), compared with Fib with high SAOS-2 labelling (b) (Mann Whitney U Test, $p < 0.0001$).* ***(c,d)*** *Proportional distribution plots binned at 2.5 kPa for stiffness and 0.2 μm for height measurements, confirmed the visual impressions from stiffness fingerprints.*

Results of numerical MATLAB simulations agreed with experimental observations

One objective of computer simulations was to determine if it was possible to explain experimental observations, applying biologically reasonable assumptions to our mathematical model. Simulations concorded well with experimental results, and also satisfied predictions of the model. Applying biologically reasonable assumptions (Figs. 3, 4), in simulations gave fluorescence transfers that closely approximated experimental fluorescence transfers (Fig. 13a,b). Median fluorescence levels of donor and receptor cells are shown in Table 1, and demonstrate similarity between experimental and simulated results, as well as proportionately more transfer from Fib to SAOS-2 than in the reverse direction. The inverse relationship between receptor cell stiffness and uptake was seen in simulations for transfer to both Fib and SAOS-2 (Fig. 13c,d).

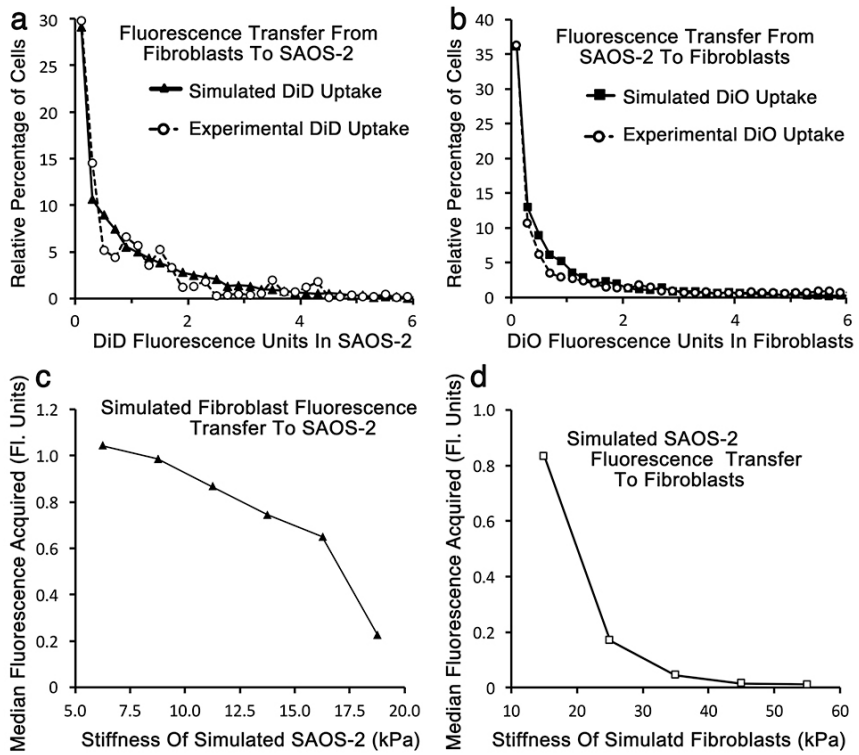

Fig. 13. *Comparison of simulated with experimentally observed transfer and the relationship between simulated recipient cell stiffness and fluorescence uptake.* ***(a,b)*** *Experimental and simulated results had good concordance where: each SAOS-2 had from 1 to 3 donor Fib (1 to 3 for Fib recipients); there were from 0 to 2 exchange events from each Fib to each SAOS-2 (3 to 8 for recipient Fib); cell-projection retraction ranged from 0.5 to 1.4 μm/s for donor Fib (1 to 5 μm/s for donor SAOS-2); the proportion of maximal possible time for individual transfer events was from 0 to 0.9 for Fib cell-projection retraction (0.6 to 0.9 for SAOS-2 cell-projection retraction); the length of donor Fib cell-projections was from 5 to 120 μm (40 to 90 μm from donor SAOS-2); the radius of Fib donor cell-projections was from 0.55 to 1.75 μm (0.7 to 2.5 μm for donor SAOS-2); and the viscosity of cytoplasm was from 1.5 to 4.0 mPa.s for both donor cells.* ***(c,d)*** *An inverse relationship between SAOS-2 stiffness and median fluorescence acquired by CPP was seen (c), with a similar result for Fib receiving SAOS-2 fluorescence (d) ($p < 0.0001$, Mann Whitney U Test).*

Calculated pressures for these simulated transfers were generally modest (for transfer from Fib to SAOS-2: median 0.58 Pa, 7.48 x 10^{-5} Pa to 4.39 Pa; for transfer from SAOS-2 to Fib: median 0.377 Pa, 8.51 x 10^{-6} Pa to 6.35 Pa). Predominantly low pressures required to account for results, support plausibility for CPP.

Table 1. Median fluorescence levels from experimental observations and simulations

	Median Fluorescence per Cell (Fluorescence Units)			Receptor Fluorescence / Donor Fluorescence	
	Donor Cells	Experimental Receptor Cells	Simulated Receptor Cells	Experimental	Simulated
Red (DiD) Fluorescence	16.904	0.641	0.630	0.038	0.037
Green (DiO) Fluorescence	31.849	0.504	0.414	0.016	0.013

Overall fluorescence levels for simulated receptor cells was comparable to that seen in experimental results. When expressed as ratios relative to donor cell fluorescence, Fib which were the receptors for green DiO fluorescence, had lower uptake relative to red DiD fluorescence by SAOS-2 receptor cells. Proportionate uptake was similar between simulation results and experimental data, with fluorescence uptake of SAOS-2 being 2.40 fold that of Fib (0.038/0.016) by experiment, and 2.81 fold that of Fib by simulation (0.037/0.013).

Simulations predicted large proportional volume transfers between cells

Donor cell fluorescence is highly variable (Figs. 2,11) (1), so that direct estimation of CPP volume transfers required to account for fluorescence levels in recipient cells was not previously possible. Nonetheless, this difficulty was overcome by the current computer simulations, where the effect of variable donor cell fluorescence was included in calculation.

Volume exchange was expressed as percentages relative to the average volume of a single Receptor Cell B, and the distribution of cells according to volumes transferred in the simulations

shown in Fig. 13, are shown in Table 2. Most simulated recipient cells accepted appreciable donor cell cytoplasm, consistent with visual impressions (1) (Figs. 6, 7, 8, 11). Amongst simulated SAOS-2, 55.5% had over 3% volume acquired from simulated Fib, and 5.2% of simulated SAOS-2 had over 19% volume acquired from simulated Fib. Consistent with occasional experimentally observed SAOS-2 with very high Fib DiD labelling, 10 simulated SAOS-2 cell acquired between 35% and 47% of their volume from simulated Fib. Proportional volume transfers to Fib were generally lower than for SAOS-2 (Table 2).

In as much as variability in donor cell fluorescence undermines direct estimation of volume transfers by CPP, the same applies for estimation of volume exchanges via shed vesicles and TNT. Nonetheless, it is not plausible that exosomes or other shed vesicles could account for the large volume transfers calculated as due to CPP in the current study. Similarly, while TNT are reported to transfer organelles, time-lapse recordings reveal such transfers to be relatively few by comparison with CPP. This is consistent with the absence of a clear mechanical motive force in TNT, as opposed to the active pumping mechanism of CPP. As such, the current simulations appear to offer the first estimation of cytoplasmic volume transfers between mammalian cells.

Limitations of modelling and simulations

Some aspects of our modeling bear further discussion. Turbulent flow is near impossible in radius values used, supporting use of the Hagen-Poiseuille relationships. Cytoplasmic viscosity is non-uniform and dependent on scale. Viscosity is low but varies across micro-volumes of the cell, dependent on contents. When measured at the whole cell level, viscosity is high due to the admixture of organelles and cytoskeletal elements (26, 27, 35). At the scale here modeled, cytoplasmic viscosity ranges upwards from that close to water to 4 mPa.s (26, 27). The effect of organelles suspended in cytoplasm is difficult to anticipate. While cytoplasm itself at the scale studied may have low viscosity in the order of 1.5 mPa.s, we have made reasonable accommodation for the effect of organelles by including higher viscosity values in simulations.

Preliminary simulations applying a normal distribution for variables other than stiffness and fluorescence, generated 'a central hump' in fluorescence profiles inconsistent with experimental fluorescence. Using a distribution with a flattened profile achieved simulation outcomes more similar to experimental results, suggesting a uniform distribution for key variables *in-vivo*. Confirmation awaits improved structural and temporal resolution of events in living cells. Modest divergence of simulated from experimental results, likely reflects limitations inherent to the model, including possible skewedness and unknown dependencies between variables.

CONCLUSIONS

The observed relationships between cell stiffness and fluorescence transfer, would not be expected if TNT or shed vesicles played a significant role, and this further supports our interpretation of CPP from time-lapse observations. Taken together, data support CPP as what seems to be a previously unrecognized mechanism for inter-cellular cytoplasmic exchange, and this report forms a reasonable theoretical framework for further investigation. CPP is in some ways similar to the hydrodynamic mechanisms described for formation of lamellipodia (36), blebbing (37, 38), and the formation of lobopodia (39).

We speculate that CPP contributes additionally to a variety of otherwise described processes, including transfer of melanosomes and mitochondria (2, 4, 5, 19, 28-30), and the development of cancer associated Fib (40).

Our earlier work showed CPP causes significant phenotypic change, including altered morphology and cytokine synthesis of recipient cells (1, 18). The inflammatory cytokine Tumor Necrosis Factor-α increased transfer from fibroblasts to SAOS-2, and this seemed due to increased binding of SAOS-2 via ICAM-1 (1, 24). One limitation of those earlier reports, was that we only studied cell phenotype in co-culture, and not cells separated after co-culture according to the extent of CPP uptake (1, 18). This is addressed in more recent work submitted elsewhere but available as a pre-print (34), in which we study MC sub-populations separated by fluorescence activated cell sorting on basis of the level of fibroblast label uptake. We found that acceptance of fibroblast marker increased MC migration and cell size (34). Internal complexity was also increased, as

Table 2. The proportionate percentage distribution of simulated recipient SAOS-2 and Fib, according to the volume acquired from the opposing cell type in simulated co-culture generating fluorescence profiles approximating those seen by experiment, expressed as percentages relative to the average volume of the respective recipient cell type (Fig. 7 of the main manuscript).

% Volume Relative to Average Recipient Cell	Simulated SAOS-2 Number	% Relative to All Simulated SAOS-2	% of Simulated SAOS-2 with Transfer over Threshold	Simulated Fibroblast Number	% Relative to All Simulated Fibroblasts	% of Simulated Fibroblasts with Transfer over Threshold
0 to < 1	1301	26.02	100	2062	41.26	100
1 to < 3	925	18.5	73.98	1274	25.46	58.74
3 to < 5	661	13.22	55.48	523	10.46	33.28
5 to < 7	455	9.1	42.26	263	5.26	22.82
7 to < 9	376	7.52	33.16	176	3.54	17.56
9 to < 11	312	6.24	25.64	135	2.58	14.02
11 to < 13	232	4.64	19.4	141	2.82	11.44
13 to < 15	205	4.1	14.76	110	2.26	8.62
15 to < 17	164	3.28	10.66	88	1.76	6.36
17 to < 19	110	2.2	7.38	80	1.6	4.6
19 to < 21	64	1.28	5.18	52	1.08	3
21 to < 23	64	1.28	3.9	26	0.52	1.92
23 to < 25	45	0.9	2.62	21	0.42	1.4
25 to < 27	23	0.46	1.72	19	0.38	0.98
27 to < 29	21	0.42	1.26	16	0.32	0.6
29 to < 31	15	0.3	0.84	4	0.08	0.28
31 to < 33	6	0.12	0.54	0	0	0.2
33 to < 35	11	0.22	0.42	3	0.06	0.2
35 to <37	3	0.06	0.2	4	0.08	0.14
37 to <39	1	0.02	0.14	0	0	0.06
39 to <41	3	0.06	0.12	2	0.04	0.06
41 to <43	0	0	0.06	0	0	0.02
43 to <45	2	0.04	0.06	0	0	0.02
45 to <47	1	0.02	0.02	0	0	0.02
47 to <49	0	0	0	1	0.02	0.02
Total	5000	100		5000	100	

Simulations predicting fluorescence profiles for recipient cells similar to experimental results (Fig. 6 of the Main Manuscript), also predicted transfer of appreciable volumes of cytoplasm to recipient cells. 55.5% of simulated SAOS-2 had over 3%, and 5.2% of SAOS-2 had over 19% volume acquired from simulated Fib. Consistent with occasional experimentally observed SAOS-2 with very high Fib DiD labelling, 10 simulated SAOS-2 cell acquired between 35% and 47% of their volume from simulated Fib. Simulated Fib also acquired appreciable cytoplasm from simulated SAOS-2, but this was generally less compared with exchange in the reverse direction.

expected from acquisition of additional organelles from fibroblasts (34). Because CPP generates sub-populations of MC with altered morphology, we suggest CPP might contribute to MC morphological diversity *in-vivo*, and hence to histopathological pleomorphism relevant to cancer diagnosis and prognosis (41). Also, since MC migration is important in cancer invasion and metastasis (41), we suggest CPP contributes to these aspects of cancer. MC diversity is central to cancer progression (41), so CPP driven MC diversity may play a role (1, 18, 34).

CPP seems mechanically more akin to intercellular exchange via TNT than via exosomes, because micro-fusions establish physical cytoplasmic continuity of neighboring cells in both TNT and CPP exchange, while exosome transfer does not require cell to cell contact. Despite this, the biological response of MC to CPP transfer of fibroblast cytoplasm in our separate work (1, 18, 34), seems more similar to the published response of cells to uptake of exosomes, than to TNT mediated transfer. For example, exosome uptake alters cell morphology (14, 15, 42), but we find no literature of TNT mediating this effect. Similarly, while exosomes from a variety of sources can increase migration of several cell types (16, 43-46), there is less evidence for a similar effect for cellular contents transferred via TNT (17). Seemingly different effects of cytoplasmic transfer by CPP and TNT, underscore the distinction between the two processes.

We have now reported CPP transfer with various melanoma, ovarian cancer, lung cancer and osteosarcoma cell lines (1, 34), while preliminary experiments suggest this also occurs between other cell types including: endothelium, smooth muscle cells and pulmonary basal cells. Cancer rarely generates new biology, but instead usually perverts established mechanisms. From this, and given altered phenotype following cytoplasmic transfer (1-17, 19), we suggest CPP may contribute to cell differentiation and phenotypic control in other biological settings including: embryogenesis, development, inflammation and wound healing.

AUTHOR CONTRIBUTIONS

HZ conceived and conducted all experiments and modelling, and prepared the manuscript. EK assisted with cell culture. NP and KM assisted with AFM, while YR, VB, SF and KM assisted with CLSM and fluorescence quantitation. GR and JC gave key input for mathematical and MATLAB modelling respectively. GWL assisted preparing movies. All authors including BC and MASM contributed to critical analysis and manuscript preparation. The authors declare no conflict of interest.

ACKNOWLEDGEMENTS

We thank the Memorial Sloan Kettering Cancer Center, including via MSKCC P30 CA008748 Cancer Center Support Grant, as well as the Australian Dental Research Fund for their support of this work. We also thank an anonymous donor for their kind contribution. We also thank Dr R Norden of the Graduate School of Biomedical Engineering, University of NSW for his advice.

SUPPLEMENTAL INFORMATION

Supplemental movies 1 to 4 are available, while legends for these movies and all MATLAB script is provided in a separate supplemental file.

REFERENCES

1. David, M. S., M. D. Huynh, E. Kelly, H. Rizos, H. Coleman, G. Rogers, and H. Zoellner. 2012. Membrane and cytoplasmic marker exchange between malignant neoplastic cells and fibroblasts via intermittent contact: increased tumour cell diversity independent of genetic change. J Pathol 228:495-505.

2. Koyanagi, M., R. P. Brandes, J. Haendeler, A. M. Zeiher, and S. Dimmeler. 2005. Cell-to-cell connection of endothelial progenitor cells with cardiac myocytes by nanotubes: a novel mechanism for cell fate changes? Circulation research 96(10):1039-1041.
3. Sinclair, K. A., S. T. Yerkovich, P. M. Hopkins, and D. C. Chambers. 2016. Characterization of intercellular communication and mitochondrial donation by mesenchymal stromal cells derived from the human lung. Stem Cell Res Ther 7(1):91.
4. Pasquier, J., B. S. Guerrouahen, H. Al Thawadi, P. Ghiabi, M. Maleki, N. Abu-Kaoud, A. Jacob, M. Mirshahi, L. Galas, S. Rafii, F. Le Foll, and A. Rafii. 2013. Preferential transfer of mitochondria from endothelial to cancer cells through tunneling nanotubes modulates chemoresistance. Journal of translational medicine 11:94.
5. Vallabhaneni, K. C., H. Haller, and I. Dumler. 2012. Vascular smooth muscle cells initiate proliferation of mesenchymal stem cells by mitochondrial transfer via tunneling nanotubes. Stem Cells Dev 21(17):3104-3113.
6. Davis, D. M., and S. Sowinski. 2008. Membrane nanotubes: dynamic long-distance connections between animal cells. Nat Rev Mol Cell Biol 9(6):431-436.
7. Gerdes, H. H., A. Rustom, and X. Wang. 2013. Tunneling nanotubes, an emerging intercellular communication route in development. Mech Dev 130(6-8):381-387.
8. Onfelt, B., S. Nedvetzki, R. K. Benninger, M. A. Purbhoo, S. Sowinski, A. N. Hume, M. C. Seabra, M. A. Neil, P. M. French, and D. M. Davis. 2006. Structurally distinct membrane nanotubes between human macrophages support long-distance vesicular traffic or surfing of bacteria. J Immunol 177(12):8476-8483.
9. Guescini, M., G. Leo, S. Genedani, C. Carone, F. Pederzoli, F. Ciruela, D. Guidolin, V. Stocchi, M. Mantuano, D. O. Borroto-Escuela, K. Fuxe, and L. F. Agnati. 2012. Microvesicle and tunneling nanotube mediated intercellular transfer of g-protein coupled receptors in cell cultures. Exp Cell Res 318(5):603-613.
10. Thayanithy, V., V. Babatunde, E. L. Dickson, P. Wong, S. Oh, X. Ke, A. Barlas, S. Fujisawa, Y. Romin, A. L. Moreira, R. J. Downey, C. J. Steer, S. Subramanian, K. Manova-Todorova, M. A. S. Moore, and E. Lou. 2014. Tumor exosomes induce tunneling nanotubes in lipid raft-enriched regions of human mesothelioma cells. Exp Cell Res 323(1):178-188.
11. Zheng, H. C. 2017. The molecular mechanisms of chemoresistance in cancers. Oncotarget 8(35):59950-59964.
12. Lou, E., S. Fujisawa, A. Barlas, Y. Romin, K. Manova-Todorova, M. A. Moore, and S. Subramanian. 2012. Tunneling Nanotubes: A new paradigm for studying intercellular communication and therapeutics in cancer. Communicative & integrative biology 5(4):399-403.
13. Ariazi, J., A. Benowitz, V. De Biasi, M. L. Den Boer, S. Cherqui, H. Cui, N. Douillet, E. A. Eugenin, D. Favre, S. Goodman, K. Gousset, D. Hanein, D. I. Israel, S. Kimura, R. B. Kirkpatrick, N. Kuhn, C. Jeong, E. Lou, R. Mailliard, S. Maio, G. Okafo, M. Osswald, J. Pasquier, R. Polak, G. Pradel, B. de Rooij, P. Schaeffer, V. A. Skeberdis, I. F. Smith, A. Tanveer, N. Volkmann, Z. Wu, and C. Zurzolo. 2017. Tunneling Nanotubes and Gap Junctions-Their Role in Long-Range Intercellular Communication during Development, Health, and Disease Conditions. Front Mol Neurosci 10:333.
14. Hood, J. L., H. Pan, G. M. Lanza, S. A. Wickline, I. Consortium for Translational Research in Advanced, and Nanomedicine. 2009. Paracrine induction of endothelium by tumor exosomes. Lab Invest 89(11):1317-1328.
15. Wu, H. H., and O. K. Lee. 2017. Exosomes from mesenchymal stem cells induce the conversion of hepatocytes into progenitor oval cells. Stem Cell Res Ther 8(1):117.
16. McCready, J., J. D. Sims, D. Chan, and D. G. Jay. 2010. Secretion of extracellular hsp90alpha via exosomes increases cancer cell motility: a role for plasminogen activation. BMC Cancer 10:294.
17. Hanna, S. J., K. McCoy-Simandle, E. Leung, A. Genna, J. Condeelis, and D. Cox. 2019. Tunneling nanotubes, a novel mode of tumor cell-macrophage communication in tumor cell invasion. J Cell Sci 132(3).
18. David, M. S., E. Kelly, and H. Zoellner. 2013. Opposite cytokine synthesis by fibroblasts in contact co-culture with osteosarcoma cells compared with transwell co-cultures. Cytokine 62(1):48-51.

19. Liu, K., K. Ji, L. Guo, W. Wu, H. Lu, P. Shan, and C. Yan. 2014. Mesenchymal stem cells rescue injured endothelial cells in an in vitro ischemia-reperfusion model via tunneling nanotube like structure-mediated mitochondrial transfer. Microvasc Res 92:10-18.
20. Ahmed, K. A., and J. Xiang. 2011. Mechanisms of cellular communication through intercellular protein transfer. J Cell Mol Med 15(7):1458-1473.
21. Ady, J. W., S. Desir, V. Thayanithy, R. I. Vogel, A. L. Moreira, R. J. Downey, Y. Fong, K. Manova-Todorova, M. A. Moore, and E. Lou. 2014. Intercellular communication in malignant pleural mesothelioma: properties of tunneling nanotubes. Frontiers in physiology 5:400.
22. Lou, E., S. Fujisawa, A. Morozov, A. Barlas, Y. Romin, Y. Dogan, S. Gholami, A. L. Moreira, K. Manova-Todorova, and M. A. Moore. 2012. Tunneling nanotubes provide a unique conduit for intercellular transfer of cellular contents in human malignant pleural mesothelioma. PLoS One 7(3):e33093.
23. Zoellner, H., N. Paknejad, K. Manova, and M. A. Moore. 2015. A novel cell-stiffness-fingerprinting analysis by scanning atomic force microscopy: comparison of fibroblasts and diverse cancer cell lines. Histochem Cell Biol 144(6):533-542.
24. David, M. S., E. Kelly, I. Cheung, M. Xaymardan, M. A. Moore, and H. Zoellner. 2014. SAOS-2 osteosarcoma cells bind fibroblasts via ICAM-1 and this is increased by tumour necrosis factor-alpha. PLoS One 9(6):e101202.
25. Barthel, E. 2008. Adhesive elastic contacts - JKR and more. Journal of Physics D: Applied Physics 41:163001-163041.
26. Fushimi, K., and A. S. Verkman. 1991. Low viscosity in the aqueous domain of cell cytoplasm measured by picosecond polarization microfluorimetry. J Cell Biol 112(4):719-725.
27. Kalwarczyk, T., N. Ziebacz, A. Bielejewska, E. Zaboklicka, K. Koynov, J. Szymanski, A. Wilk, A. Patkowski, J. Gapinski, H. J. Butt, and R. Holyst. 2011. Comparative analysis of viscosity of complex liquids and cytoplasm of mammalian cells at the nanoscale. Nano letters 11(5):2157-2163.
28. Scott, G., S. Leopardi, S. Printup, and B. C. Madden. 2002. Filopodia are conduits for melanosome transfer to keratinocytes. J Cell Sci 115(Pt 7):1441-1451.
29. Singh, S. K., R. Kurfurst, C. Nizard, S. Schnebert, E. Perrier, and D. J. Tobin. 2010. Melanin transfer in human skin cells is mediated by filopodia--a model for homotypic and heterotypic lysosome-related organelle transfer. FASEB J 24(10):3756-3769.
30. Ma, H. J., H. Y. Ma, Y. Yang, P. C. Li, S. X. Zi, C. Y. Jia, and R. Chen. 2014. alpha-Melanocyte stimulating hormone (MSH) and prostaglandin E2 (PGE2) drive melanosome transfer by promoting filopodia delivery and shedding spheroid granules: Evidences from atomic force microscopy observation. J Dermatol Sci 76(3):222-230.
31. Darby, R., and R. P. Chhabra. 2016. Chemical engineering fluid mechanics. CRC Press, Boca Raton, FL.
32. Law, J., and R. Rennie. 2009. A dictionary of physics. In A dictionary of physics. J. Law and R. Rennie, editors. Oxford University Press, Oxford.
33. Feneberg, W., M. Westphal, and E. Sackmann. 2001. Dictyostelium cells' cytoplasm as an active viscoplastic body. Eur Biophys J 30(4):284-294.
34. Zoellner, H., B. Chami, E. Kelly, and M. A. Moore. 2019. Increased cell size, structural complexity and migration of cancer cells acquiring fibroblast organelles by cell-projection pumping. . bioRxiv http://dx.doi.org/10.1101/770693.
35. Plaza, G. R., N. Mari, B. G. Galvez, A. Bernal, G. V. Guinea, R. Daza, J. Perez-Rigueiro, C. Solanas, and M. Elices. 2014. Simple measurement of the apparent viscosity of a cell from only one picture: Application to cardiac stem cells. Phys Rev E Stat Nonlin Soft Matter Phys 90(5-1):052715.
36. Manoussaki, D., W. D. Shin, C. M. Waterman, and R. S. Chadwick. 2015. Cytosolic pressure provides a propulsive force comparable to actin polymerization during lamellipod protrusion. Scientific reports 5:12314.
37. Charras, G. T., J. C. Yarrow, M. A. Horton, L. Mahadevan, and T. J. Mitchison. 2005. Non-equilibration of hydrostatic pressure in blebbing cells. Nature 435(7040):365-369.
38. Strychalski, W., and R. D. Guy. 2016. Intracellular Pressure Dynamics in Blebbing Cells. Biophys J 110(5):1168-1179.

39. Petrie, R. J., N. Gavara, R. S. Chadwick, and K. M. Yamada. 2012. Nonpolarized signaling reveals two distinct modes of 3D cell migration. J Cell Biol 197(3):439-455.
40. LeBleu, V. S., and R. Kalluri. 2018. A peek into cancer-associated fibroblasts: origins, functions and translational impact. Dis Model Mech 11(4).
41. Kumar, V., and A. K. Abbas. 2014. Robbins and Cotran pathologic basis of disease. Elsevier Saunders, Philadelphia, Penn.
42. Morton, M. C., V. N. Neckles, C. M. Seluzicki, J. C. Holmberg, and D. M. Feliciano. 2018. Neonatal Subventricular Zone Neural Stem Cells Release Extracellular Vesicles that Act as a Microglial Morphogen. Cell Rep 23(1):78-89.
43. Gastpar, R., M. Gehrmann, M. A. Bausero, A. Asea, C. Gross, J. A. Schroeder, and G. Multhoff. 2005. Heat shock protein 70 surface-positive tumor exosomes stimulate migratory and cytolytic activity of natural killer cells. Cancer Res 65(12):5238-5247.
44. Cheng, C. F., J. Fan, M. Fedesco, S. Guan, Y. Li, B. Bandyopadhyay, A. M. Bright, D. Yerushalmi, M. Liang, M. Chen, Y. P. Han, D. T. Woodley, and W. Li. 2008. Transforming growth factor alpha (TGFalpha)-stimulated secretion of HSP90alpha: using the receptor LRP-1/CD91 to promote human skin cell migration against a TGFbeta-rich environment during wound healing. Mol Cell Biol 28(10):3344-3358.
45. Samaeekia, R., B. Rabiee, I. Putra, X. Shen, Y. J. Park, P. Hematti, M. Eslani, and A. R. Djalilian. 2018. Effect of Human Corneal Mesenchymal Stromal Cell-derived Exosomes on Corneal Epithelial Wound Healing. Invest Ophthalmol Vis Sci 59(12):5194-5200.
46. Nakamura, K., K. Sawada, Y. Kinose, A. Yoshimura, A. Toda, E. Nakatsuka, K. Hashimoto, S. Mabuchi, K. I. Morishige, H. Kurachi, E. Lengyel, and T. Kimura. 2017. Exosomes Promote Ovarian Cancer Cell Invasion through Transfer of CD44 to Peritoneal Mesothelial Cells. Mol Cancer Res 15(1):78-92.